nature materials

Supplementary information

https://doi.org/10.1038/s41563-026-02759-4

Bioresorbable metal-free molecular magnets enable untethered organ monitoring

In the format provided by the authors and unedited

The PDF file includes:

Supplementary Notes 1-4
Supplementary Figures 1-51
Supplementary Tables 1-4
Supplementary Legends for Videos 1-6
Supplementary References

Other Supplementary Materials for this manuscript include the following:

Supplementary Videos 1-6

Supplementary Note 1 | Computational framework and theoretical mechanism of spontaneous magnetization in BioMFM
Supplementary Note 2 | Geometric–Textual Model for Per-Atom Magnetic-Moment Prediction (FT-ChemBERTa)
Supplementary Note 3 | Engineering Reliability and Bioresorption of Bloomable BioMFM Implants
Supplementary Note 4 | The Physics Aware Gaussian Optimization for Low-resolution Discrete Source Magnetic Field Decomposition (PAGO-DeMag) Algorithm
Supplementary Figure 1 | Controlled thermal synthesis and structural evolution of BioMFM
Supplementary Figure 2 | Morphological and compositional characterization of BioMFM and precursor g-C_3N_4
Supplementary Figure 3 | Synchrotron XANES spectra resolving element-specific electronic structure and framework reconstruction
Supplementary Figure 4 | Longitudinal EPR tracking and ambient stability of framework radical centers
Supplementary Figure 5 | Element-specific spin polarization and magnetic domain configurations of BioMFM
Supplementary Figure 6 | Macroscopic magnetometry, synthetic reproducibility, and high-temperature ferromagnetic phase transitions of BioMFM
Supplementary Figure 7 | Nanomechanical profiling and long-term colloidal stability tracking of BioMFM
Supplementary Figure 8 | Theoretical electronic structures and relaxed atomic configurations of g-C_3N_4 derivatives
Supplementary Figure 9 | Evolution of electronic structure and magnetic moments with increasing C-C• concentration
Supplementary Figure 10 | Bader charge distribution of the pristine g-C_3N_4
Supplementary Figure 11 | Orbital-resolved electronic structure and bonding stabilization in the C-C• defect region
Supplementary Figure 12 | Site-specific electronic states and orbital-resolved bonding stabilization at the C-C• defect
Supplementary Figure 13 | Local bonding motifs and nearest-neighbor environments in the BioMFM-C-C•$_4$
Supplementary Figure 14 | Orbital-resolved bonding analysis and electronic states at the C3 site
Supplementary Figure 15 | Orbital-resolved bonding analysis and electronic states at the C11 site
Supplementary Figure 16 | Orbital-resolved bonding analysis and electronic states at the C23 site
Supplementary Figure 17 | Orbital-resolved bonding analysis and electronic states at the N25 site
Supplementary Figure 18 | Evolution of spin-polarized electronic band structures with increasing C-C• multiplicity
Supplementary Figure 19 | Spin-unpolarized density of states and spatial spin-density distributions for high-density defect configurations
Supplementary Figure 20 | Architecture and implementation of the FT-ChemBERTa model for atom-resolved magnetic moment prediction

Supplementary Figure 21 | Spatial error distribution and interpretability of FT-ChemBERTa magnetic moment predictions
Supplementary Figure 22 | Thermo-hygroscopic characterization and actuation of the silk-fibroin robotic layer
Supplementary Figure 23 | Computational modeling of mechanical reliability and deployment kinematics of the BioMFM patch
Supplementary Figure 24 | Structural memory longevity and cyclic relocation fatigue boundaries of the BioMFM patch
Supplementary Figure 25 | Nanomechanical compliance and high-cycle interfacial durability of the BioMFM patch
Supplementary Figure 26 | Degradation pathways, cytocompatibility profiles, and multi-environment clearance kinetics of the BioMFM scaffold
Supplementary Figure 27 | Comprehensive in vitro cytocompatibility and early-stage in vivo histocompatibility of magnetic biomaterials
Supplementary Figure 28 | Structural configurations and fabrication paradigms of BioMFM and inorganic composite patches
Supplementary Figure 29 | In vivo echocardiographic evaluation and mechanical safety profiling of baseline cardiac function
Supplementary Figure 30 | Computational modeling of magneto-mechanical transduction across the cardiac cycle
Supplementary Figure 31 | System-level architecture and cloud-integrated pipeline of the wearable BioMFM reader
Supplementary Figure 32 | Hardware architecture and signal characterization of the wearable Hall-effect sensing system
Supplementary Figure 33 | Computational validation of the PAGO-DeMag algorithm for motion-robust cardiac reconstruction
Supplementary Figure 34 | Workflow and dynamic implementation of the PAGO-DeMag algorithm for cardiac volumetry
Supplementary Figure 35 | Quantitative sensitivity analysis of the PAGO-DeMag algorithm against geometric, calibration, and noise-induced sensor non-idealities
Supplementary Figure 36 | Machine-learning pipeline for rhythm classification from BioMFM-derived volumetric traces
Supplementary Figure 37 | Rhythm classification performance from BioMFM-derived volumetric traces
Supplementary Figure 38 | Algorithmic robustness and signal integrity of PAGO-DeMag under partial magnetic source dropout
Supplementary Figure 39 | Co-planar hardware loop and dynamic common-mode vector field cancellation for ambulatory geomagnetic noise suppression
Supplementary Figure 40 | In vivo MRI validation of BioMFM epicardial placement and longitudinal stability
Supplementary Figure 41 | Longitudinal systemic biosafety and histopathological evaluation of BioMFM implants
Supplementary Figure 42 | Longitudinal all-day cardiac volumetric monitoring across the perioperative window
Supplementary Figure 43 | Conventional echocardiographic characterization and functional snapshots in the porcine MI model
Supplementary Figure 44 | Longitudinal correlation of ejection fraction (EF) measurements between the BioMFM platform and clinical echocardiography
Supplementary Figure 45 | Quantitative evaluation of the minimum detectable displacement boundary and cyclic sensitivity profiles
Supplementary Figure 46 | Density functional theory modeling of spin-state environmental tolerance
Supplementary Figure 47 | Thermoresponsive wettability and hydration-dependent surface

characteristics of BioMFM-PNIPAM hydrogels
Supplementary Figure 48 | Thermoresponsive magnetic domain reconfiguration and structural evolution in BioMFM-PNIPAM hydrogels
Supplementary Figure 49 | Electrokinetic profiles and ambient EPR spin-state simulations
Supplementary Figure 50 | Stimuli-responsive rheological transitions and network reversibility of the hydrogel matrices
Supplementary Figure 51 | Multimodal glucose-responsive magnetic reconfiguration and rheological characterization of BioMFM hydrogels
Supplementary Table 1 | Comparative benchmarking of the BioMFM system against predominant bioelectronic monitoring modalities
Supplementary Table 2 | Elemental composition of BioMFM determined by inductively coupled plasma–optical emission spectroscopy (ICP-OES)
Supplementary Table 3 | Comparison of Curie temperature and saturation magnetization for representative metal-free molecular ferromagnets and metallic inorganic ferromagnets
Supplementary Table 4 | *Stoner* analysis of itinerant ferromagnetism in BioMFM-C–C•$_x$ motifs
Supplementary Video 1 | Macroscopic demonstration of spontaneous room-temperature ferromagnetism in BioMFM
Supplementary Video 2 | Bloomable BioMFM implant transitioning from closed delivery state to deployed configuration
Supplementary Video 3 | Continuous spatiotemporal myocardial dynamic mapping with a BioMFM system
Supplementary Video 4 | MRI verification (Day 28) of stable epicardial BioMFM implant deployed on a porcine myocardium
Supplementary Video 5 | Ultrasound-guided percutaneous injection of BioMFM hydrogel
Supplementary Video 6 | Injectability and filament extrusion of BioMFM–sodium-alginate hydrogel

Supplementary Note 1: Computational framework and theoretical mechanism of spontaneous magnetization in BioMFM

This Supplementary Note provides the detailed electronic-structure analysis underlying the condensed mechanistic discussion in the main text, including defect-dependent magnetic ground states, charge redistribution, orbital-resolved bonding, and Stoner analysis across extended BioMFM configurations.

De-nitrogenation-induced Magnetic Ground State

Within this computational framework, pristine graphitic carbon nitride (g-C_3N_4) is intrinsically nonmagnetic because its spin-up and spin-down states are fully compensated. Incorporation of hydroxyl groups does not alter this nonmagnetic character. By contrast, de-nitrogenation introduces C–C• radical centres and pronounced spin asymmetry near the Fermi level (E_F), resulting in uncompensated spin polarization and the onset of magnetism. The de-nitrogenated g-C_3N_4 framework is herein referred to as the bioresorbable metal-free molecular magnet BioMFM.

Structural relaxation further shows that de-nitrogenation reconstructs the nearly planar g-C_3N_4 lattice into a corrugated π–σ conjugated framework with a local tilt of ~31.2° containing C–C• radical centres together with hydroxyl (–OH) and cyano (–C≡N) terminations. Density-of-states calculations indicate that stoichiometric and –OH/–C≡N-terminated configurations remain nonmagnetic, whereas structures containing C–C• centres develop pronounced spin asymmetry near E_F, dominated by 2p-derived electronic states. Energetic comparisons between magnetic configurations further show that the ferromagnetic (FM) state is energetically more favourable than the antiferromagnetic (AFM) state, establishing FM ordering as the preferred magnetic ground state of C–C•-containing BioMFM configurations.

The C–C• concentration plays an important role in determining the resulting magnetic moment. Across BioMFM–C–C•$_x$ configurations, additional radical centres introduce defect states near E_F and progressively modify the electronic landscape. The calculated magnetic moment does not evolve monotonically with C–C• concentration because it is sensitive not only to the number of defects but also to their spatial arrangement within the reconstructed framework. Configurations with x = 1-6 retain finite magnetic moments, whereas excessive de-nitrogenation eventually perturbs the electronic structure and suppresses spin polarization. These calculations identify de-nitrogenation-induced C–C• states as the fundamental origin of magnetism in the π–σ conjugated BioMFM framework.

Charge Redistribution and Localized–itinerant 2p States

To clarify how local defect chemistry evolves into long-range magnetic coupling, we analysed the charge distribution using Bader partitioning. In pristine g-C_3N_4, valence charge is strongly concentrated around nitrogen-rich regions, consistent with its nonmagnetic ground state. Removal of nitrogen reconstructs the lattice from a predominantly π-conjugated C–N framework into the π–σ conjugated BioMFM structure and reduces the local polarity of neighbouring C–N bonds. The corresponding charge redistribution transfers electronic density from N-rich regions into the reconstructed conjugated network, increasing the delocalized character of the 2p electrons.

The resulting defect-associated states exhibit a mixed localized–itinerant character. Their localized 2p component establishes spin-polarized centres around specific C–C• motifs, whereas hybridization between neighbouring sites produces narrow electronic bands with finite dispersion near E_F. This finite dispersion, together with favourable energetic positioning near the Fermi level, enables intersite exchange and spin splitting. BioMFM magnetism is therefore not described by completely isolated molecular radicals; instead, the C–C• defects generate locally concentrated spin centres that are electronically coupled through itinerant 2p states distributed across the reconstructed π–σ framework. This localized–itinerant character provides the link between de-nitrogenation-induced defect chemistry and long-range ferromagnetic order.

Orbital-resolved Origin of Exchange Coupling

Orbital-resolved electronic-structure calculations identify the out-of-plane P_z channel as the dominant contribution to these itinerant magnetic states. Spin-resolved density-of-states calculations at representative N and C sites exhibit pronounced splitting near E_F, with substantial contributions from P_z-character states.

To quantify the bonding character of these states, integrated crystal orbital Hamilton population (ICOHP) analysis was performed for representative atomic pairs. The P_z-mediated interactions exhibit substantially weaker bonding stabilization than the corresponding s, P_x, and P_y channels, leaving partially occupied or antibonding electronic weight close to E_F. At representative N15- and C11-centred environments, this trend is consistently observed, supporting the assignment of P_z orbitals as the principal channel hosting the itinerant 2p electrons.

We further examined whether this orbital picture persists across chemically distinct local environments by analysing the C3, C11, C23 and N25 sites within the BioMFM–C–C•$_4$ configuration (**Supplementary Figures 13–17**). Orbital-resolved COHP calculations across these representative motifs show that the P_z channel generally retains comparatively weak bonding stabilization together with pronounced antibonding weight near E_F. These site-resolved calculations therefore support a framework-wide electronic picture in which partially unpaired itinerant P_z electrons connect defect-associated spin centres and provide the primary pathway for site-to-site exchange coupling through the reconstructed π–σ network.

The near-E_F states also exhibit substantial antibonding character. Because occupation of antibonding states is energetically sensitive to exchange splitting, redistribution of these states between majority- and minority-spin channels can lower the total electronic energy. The combination of a high density of P_z-derived states near E_F, partial antibonding occupation and finite band dispersion therefore favours exchange-driven spin polarization and stabilizes the ferromagnetic ground state.

Stoner-type Spin-splitting Instability

The stability of this itinerant ferromagnetic state can be further rationalized within the Stoner framework. Within spin-polarized Kohn–Sham DFT[1], the exchange splitting of a band n at wavevector $\boldsymbol{k}$ is

$$\Delta_{n\boldsymbol{k}} = \varepsilon_{n\boldsymbol{k}} \uparrow - \varepsilon_{n\boldsymbol{k}} \downarrow$$

A site-averaged *Stoner* parameter I_s can be estimated as

$$I_s \approx \frac{< \Delta_{n\boldsymbol{k}} >_{E_F}}{\Delta_m} \ (\mathrm{eV}/\mu_\mathrm{B})$$

where $<>_{E_F}$ denotes an average over bands/states crossing E_F, and Δ_m is the per-atom net moment obtained by distributing the cell moment over C/N sites.

The *Stoner* factor

$$\mathrm{S} = I_s N(E_F)$$

gauges proximity to itinerant ferromagnetism (criterion $\mathrm{S} > 1$)[2].

For BioMFM-C-C•$_2$, the exchange splitting is $|\Delta_{n\boldsymbol{k}}| \approx 0.35\ \mathrm{eV}$, yielding $\mathrm{S} = 8.04 > 1$, consistent with robust spontaneous magnetization observed experimentally. Extending this analysis across BioMFM-C-C•$_x$ (**Supplementary Table 4**), configurations with x = 1-6 exhibit $S > 1$ and spin-polarized bands at E_F (**Supplementary Figure 18**), whereas excessive C-C• configurations (x = 7) destabilize the lattice and suppress the moment.

These results are consistent with the orbital-resolved picture described above: C–C•-induced reconstruction produces a sufficiently large near-E_F density of itinerant 2p-derived states, particularly in the P_z channel, such that exchange splitting lowers the total energy and stabilizes spontaneous

ferromagnetic order.

Robustness across Extended Defect Concentrations

To test whether the same mechanism remains applicable beyond the defect concentrations used in the primary structural models, we additionally analysed highly defect-rich BioMFM–C–C•$_8$ and BioMFM–C–C•$_9$ configurations. Their electronic structures retain pronounced near-E_F DOS features and remain consistent with the same Stoner-type spin-splitting framework (**Supplementary Figure 19**). The corresponding real-space spin-density distributions further show that these high-defect-density configurations do not require an additional or independent magnetic mechanism. Instead, their magnetic behaviour remains governed by C–C•-induced 2p-electron spin polarization within the reconstructed π–σ framework.

Mechanistic Summary

Together, the calculations establish a hierarchical mechanism for spontaneous magnetization in BioMFM. De-nitrogenation generates C–C• radical centres and reconstructs the π-conjugated g-C_3N_4 precursor into a π–σ network. These defects redistribute valence charge and generate partially localized but electronically coupled 2p states. Orbital-resolved calculations identify near-E_F P_z-derived antibonding states as the principal itinerant channel linking local spin centres, while the resulting density of states and exchange splitting satisfy the Stoner criterion across a broad range of C–C• configurations. BioMFM ferromagnetism can therefore be described as C–C•-induced 2p-electron itinerant ferromagnetism stabilized by exchange splitting within the reconstructed π–σ conjugated framework.

Supplementary Note 2: Geometric–Textual Model for Per-Atom Magnetic-Moment Prediction (FT-ChemBERTa)

We consider a dataset of BioMFM-related molecules whose heavy atoms lie in the alphabet ($\mathcal{A} = \{\mathrm{C}, \mathrm{N}, \mathrm{O}\}$). For each molecule with N atoms, we are given an $N \times 6$ array X whose i-th row is the feature vector $\boldsymbol{x}_i = [\boldsymbol{e}_i^{\top}, \boldsymbol{p}_i^{\top}] \in \mathbb{R}^6$. Here $e_i \in \{0,1\}^3$ is the one-hot encoding of the element $\boldsymbol{a}_i \in \mathcal{A}$ and $\boldsymbol{p}_i = (x_i, y_i, z_i) \in \mathbb{R}^3$ are Cartesian coordinates. Per-atom scalar targets are provided separately as the vector $\boldsymbol{m} = (m_1, \ldots, m_N) \in \mathbb{R}^N$. We also obtained the SMILES[3] string s for the same molecule, which was generated directly from structural information, with both atom types and bond relationships derived from DFT calculations. Unless stated otherwise, we make the following assumptions: i) Consistency. The CSV enumerates the same heavy-atom ordering as the canonical SMILES used by ChemBERTa; if not, a fixed permutation π aligning CSV indices to SMILES indices is known and applied. ii) Rigidity. Coordinates are in a single conformer; absolute orientation and translation are arbitrary. iii) Bounded geometry. For each molecule, the interatomic distances are finite, and the molecular graph is connected.

Let $\boldsymbol{p}_i = (x_i, y_i, z_i)^{\top}$ and N be the number of atoms. We remove translation and isotropically scale the configuration as follows:

$$\text{(T)} \quad \boldsymbol{\mu} = \frac{1}{N}\sum_{i=1}^{N} \mathbf{p}_i, \qquad \mathbf{p}_i^{(0)} = \mathbf{p}_i - \boldsymbol{\mu}.$$

$$\text{(S)} \quad s = \left(\frac{1}{N}\sum_{i=1}^{N} \| \mathbf{p}_i^{(0)} \|_2^2\right)^{1/2}, \qquad \tilde{\mathbf{p}}_i = \mathbf{p}_i^{(0)}/s.$$

Step (T) makes the representation translation-invariant. Step (S) fixes a canonical length scale and prevents trivial collapse under degenerate diameter. To verify rotation invariance of the subsequent neighborhood construction and features, consider a rigid motion $\boldsymbol{p}_i \mapsto R\boldsymbol{p}_i + \boldsymbol{t}$ with $R \in SO(3)$ and $\boldsymbol{t} \in \mathbb{R}^3$. Then

$$\boldsymbol{\mu}' = \frac{1}{N}\sum_i (R\boldsymbol{p}_i + \boldsymbol{t}) = R\boldsymbol{\mu} + \boldsymbol{t}, \quad \boldsymbol{p}_i^{(0)\prime} = R\boldsymbol{p}_i^{(0)}.$$

Because $\|R\boldsymbol{v}\|_2 = \|\boldsymbol{v}\|_2$, we have

$$s' = \left(\frac{1}{N}\sum_i \left\|\boldsymbol{p}_i^{(0)\prime}\right\|_2^2\right)^{\frac{1}{2}} = \left(\frac{1}{N}\sum_i \left\|\boldsymbol{p}_i^{(0)}\right\|_2^2\right)^{\frac{1}{2}} = s,$$

and hence $\tilde{\boldsymbol{p}}_i' = R\tilde{\boldsymbol{p}}_i$. All pairwise distances $\left\|\tilde{\boldsymbol{p}}_i - \tilde{\boldsymbol{p}}_j\right\|_2$ are unchanged, so any neighborhood defined by these distances is rotation-invariant. Rotational robustness of the overall model is further promoted by random-rotation augmentation. Thereafter, we apply data augmentation including random rotations, reflections, and small Gaussian jitter $\epsilon \sim \mathcal{N}(0, \sigma^2 I_3)$ with $\sigma \ll 1$, followed by re-normalization via (T)-(S).

Given normalized coordinates $\{\tilde{\boldsymbol{p}}_i\}_{i=1}^N$, we form a radius graph with cutoff $r_{\mathrm{cut}} > 0$ and extract fixed-size local segments of K atoms to serve as inputs to the per-atom regressor.

$$E = \left\{(i,j) \in [N]^2 : i \neq j,\ \left\|\tilde{\boldsymbol{p}}_i - \tilde{\boldsymbol{p}}_j\right\|_2 \leq r_{\mathrm{cut}}\right\}.$$

We encode element types with the one-hot basis,

$$\boldsymbol{e}_i = (1[a_i = \mathrm{C}],\ 1[a_i = \mathrm{N}],\ 1[a_i = \mathrm{O}]).$$

The node feature for atom i is

$$\boldsymbol{x}_i = \begin{bmatrix} \boldsymbol{e}_i \\ \widetilde{\boldsymbol{p}}_i \end{bmatrix} \in \mathbb{R}^6.$$

For segment $\mathcal{S}_i = \{j_1, \dots, j_K\}$, we assemble

$$X_i = \begin{bmatrix} \mathbf{x}_{j_1}^\top \\ \vdots \\ \mathbf{x}_{j_K}^\top \end{bmatrix} \in \mathbb{R}^{K\times 6}, \qquad \mathbf{y}_i = \begin{bmatrix} m_{j_1} \\ \vdots \\ m_{j_K} \end{bmatrix} \in \mathbb{R}^K.$$

Across the full dataset containing M atoms, we compute the mean and standard deviation:

$$\mu_m = \frac{1}{M}\sum_{\ell=1}^{M} m_\ell\,, \qquad \sigma_m = \left(\frac{1}{M}\sum_{\ell=1}^{M}(m_\ell - \mu_m)^2\right)^{\frac{1}{2}},$$

and standardize segment targets

$$\widetilde{\boldsymbol{y}}_i = \frac{\boldsymbol{y}_i - \mu_m \mathbf{1}}{\sigma_m} \in \mathbb{R}^K.$$

Standardization stabilizes optimization and permits a single learning rate across molecules with widely different units or scales; at inference time, predictions are mapped back by $\widehat{\boldsymbol{y}}_i^{(\mathrm{orig})} = \sigma_m \widehat{\boldsymbol{y}}_i + \mu_m$.

Let $s = (c_1, \dots, c_T)$ be the SMILES string associated with the row set. We apply ChemBERTa's byte-level BPE tokenizer to obtain token IDs $(t_1, \dots, t_L)$, with sentinel tokens ([BOS], [EOS]) and attention mask $\boldsymbol{m} \in \{0,1\}^L$. The ChemBERTa encoder maps these to hidden states $H \in \mathbb{R}^{L\times d}$. We form a global molecular embedding by masked mean pooling

$$\boldsymbol{z} = \frac{1}{\sum_{\ell=1}^{L} m_\ell}\sum_{\ell=1}^{L} m_\ell\, H_{\ell\cdot} \in \mathbb{R}^d.$$

To inject this textual context into the geometric segment, we compute a context vector $\boldsymbol{c} = U\boldsymbol{z} + \boldsymbol{b} \in \mathbb{R}^q$ with trainable $(U, \boldsymbol{b})$. Broadcast to every row and construct

$$\hat{X}_i = [\, X_i \;\; \mathbf{1}_K \mathbf{c}^\top \,] \in \mathbb{R}^{K\times(6+q)}.$$

Let f_θ be the per-segment regressor operating on $(\hat{X}_i, E_i)$, producing per-position predictions $\widehat{\boldsymbol{y}}_i = f_\theta(\hat{X}_i, E_i) \in \mathbb{R}^K$. For a minibatch of B segments, we stack

$$\hat{X} \in \mathbb{R}^{B\times K\times d_x}, \quad W \in \{0,1\}^{B\times K}, \quad \tilde{Y} \in \mathbb{R}^{B\times K}, \quad \hat{Y} = f_\theta(\hat{X}, \mathcal{E}),$$

where $d_x = 6 + q$, W contains the masks, and $\mathcal{E}$ collects per-segment edge lists. We minimize the masked mean-squared error

$$\mathcal{L}_{\mathrm{MSE}}(\theta) = \frac{1}{\sum_{b=1}^{B}\sum_{r=1}^{K} W_{br}}\sum_{b=1}^{B}\sum_{r=1}^{K} W_{br}\,(\hat{Y}_{br} - \tilde{Y}_{br})^2.$$

Regularization terms $\gamma(\boldsymbol{z})$ and $\beta(\boldsymbol{z})$ can be added explicitly if desired. For instance,

$$\mathcal{L} = \mathcal{L}_{\mathrm{MSE}} + \lambda_\gamma \mathbb{E}[\|\gamma(\boldsymbol{z}) - \mathbf{1}\|_2^2] + \lambda_\beta \mathbb{E}[\|\beta(\boldsymbol{z})\|_2^2].$$

Supplementary Note 3: Engineering Reliability and Bioresorption of Bloomable BioMFM Implants

This Supplementary Note provides detailed engineering and degradation characterization underlying the condensed discussion of the bloomable BioMFM implant in the main text, including deployment mechanics, long-term structural reliability, interfacial mechanical compliance and programmed bioresorption.

Engineering Reliability of the Bloomable Architecture

The bloomable BioMFM implant was designed to increase the effective tissue–device contact area while maintaining a small delivery footprint for minimally invasive implantation. The trilayer architecture comprises a poly(lactic-co-glycolic acid) (PLGA) mechanical backbone, a BioMFM magnetic layer and a silk-fibroin actuation/adhesion layer. The PLGA layer provides structural support during delivery and implantation, whereas the BioMFM layer serves as the passive magnetic source for deep-tissue sensing. The silk-fibroin component undergoes thermally induced deformation during deployment and subsequently hydrates to form a conformal wet adhesive, enabling sutureless attachment to dynamic tissue surfaces (**Supplementary Figure 22**).

The four-petal configuration enables the implant to transition between a compact folded state and an expanded deployed state. During delivery, the petals are constrained within the sheath to minimize the implantation footprint. Upon release at the target site, the petals recover their expanded configuration, thereby increasing the effective tissue-contact area. Hydration-induced softening and liquefaction of the silk-fibroin base subsequently mechanically decouple the four petals, allowing each petal to conform independently to local tissue curvature and dynamic organ topography.

Finite-element analysis indicates that mechanical deformation during blooming is concentrated predominantly at the hinge and folding regions (maximum $\varepsilon_{\mathrm{VMS}} \leq 5.8 \times 10^{-2}$), whereas strain across the functional petal surfaces remains comparatively low (**Supplementary Figure 23**). This distribution reduces mechanical loading of the magnetic functional layer during deployment. Longitudinal characterization further shows that the bloomable architecture preserves its structural integrity and deployment kinematics after 35 days of ambient storage and maintains reproducible elastic recovery across repeated delivery–release–retrieval cycles (**Supplementary Figure 24**).

Mechanical testing of the deployed configuration further demonstrates that petal decoupling minimizes parasitic mechanical loading on the underlying compliant substrate. The implant introduces a force of approximately 0.002 N at 10% strain and retains stable interfacial cohesion during repeated deformation. High-cycle stretch–relaxation measurements show no macroscopic delamination or progressive mechanical failure during prolonged cyclic loading (**Supplementary Figure 25**). Together, these results demonstrate that the bloomable architecture combines compact catheter-compatible delivery with mechanically compliant integration on deformable tissue surfaces.

Bioresorption and Degradation Behavior

The trilayer implant was designed with staggered degradation kinetics to provide mechanical and magnetic functionality over the perioperative monitoring window followed by progressive clearance. In phosphate-buffered saline (PBS; pH 7.4, 37 °C), the three constituent layers exhibit distinct degradation behaviors.

Silk fibroin rapidly hydrates after exposure to the aqueous environment, transitioning into an adhesive hydrogel within approximately 6–7 s before undergoing subsequent resorption. This rapid hydration simultaneously enables wet adhesion and mechanical decoupling of the individual petals. PLGA undergoes substantially slower hydrolytic degradation, providing a week-scale structural backbone and

remaining partially present at approximately 56 days. By contrast, the BioMFM layer progressively fragments and approaches near-complete disappearance by approximately 44 days.

The degradation of BioMFM is consistent with oxidation-assisted cleavage of C–N bonds within the reconstructed π–σ conjugated framework, resulting in progressive deconjugation and fragmentation of the molecular structure. The resulting degradation pathway yields increasingly small C- and N-containing species that can undergo further physiological processing. Throughout the monitored degradation period, the surrounding aqueous microenvironment remains close to physiological pH, changing only from approximately 7.4 to 7.3 (**Supplementary Figure 26**).

In vivo gross-morphological observations further corroborate progressive loss of implant material over time, consistent with the degradation behaviour observed under aqueous incubation conditions. The combined degradation profiles of silk fibroin, PLGA and BioMFM therefore provide a temporally staggered pathway in which rapid deployment and adhesion are followed by sustained mechanical support and magnetic functionality, and ultimately by progressive implant clearance.

Supplementary Note 4: The Physics Aware Gaussian Optimization for Low-resolution Discrete Source Magnetic Field Decomposition (PAGO-DeMag) Algorithm

The goal of the Physics Aware Gaussian Optimization for Low-resolution Discrete Source Magnetic Field Decomposition (PAGO-DeMag) Algorithm is to decompose low-resolution "image" of magnetic fields and reconstruct the spatial position of each magnet with high accuracy. We further divide the problem into two subproblems: to decompose the spatial position in the plane parallel to the plane of the sensor array (hence, the xy plane) and the orthogonal distance from the sensor plane (z-axis position).

To reconstruct the position in the xy plane and recover the z axis position, we employed a three-step approach: interpolation, iterative Gaussian inhibition and non-linear position optimization using Gaussians as a strong prior. The estimation of magnetic field distribution as a Gaussian in both the inhibition and position optimization steps is supported by the physics of magnetism and sensor principles.

We start our derivation from the magnetic field of a small dipole

$$\vec{B}(\vec{r}) = \frac{\mu_0}{4\pi} \cdot \left(\frac{3\hat{r}(\vec{m} \cdot \hat{r}) - \vec{m}}{|\vec{r}|^3} \right) = \frac{\mu_0}{4\pi} \cdot \left(\frac{3\vec{r}(\vec{m} \cdot \vec{r})}{|\vec{r}|^5} - \frac{\vec{m}}{|\vec{r}|^3} \right)$$

Because the sensor measures only the vertical field component, decomposition in the measurement-relevant z-direction in cylindrical coordinates gives:

$$\overrightarrow{B_z}(\vec{\rho}, z_0) = \frac{\mu_0}{4\pi} \cdot \left(\frac{3z_0^2}{(|\vec{\rho}|^2 + z_0^2)^{\frac{5}{2}}} - \frac{1}{(|\vec{\rho}|^2 + z_0^2)^{\frac{3}{2}}} \right) = \frac{\mu_0}{4\pi} \cdot \left(\frac{2z_0^2 - \rho^2}{(|\vec{\rho}|^2 + z_0^2)^{\frac{5}{2}}} \right)$$

To understand the effect of the sensor array on the perceived magnetic field, we evaluate the frequency domain of the magnetic field of a small dipole. Namely, we employ Hankel transformation to decompose the field into Bessel functions of the first kind.

$$\tilde{f}(k) = 2\pi \int_0^\infty f(\rho) J_0(k\rho) \rho d\rho$$

where J_0 are zero-order Bessel functions of the first kind.

Decomposing the magnetic field in the measurement-relevant z-direction in cylindrical coordinates yields

$$\widetilde{B_z}(k) = 2\pi \int_0^\infty \left(\frac{\mu_0}{4\pi} \cdot \frac{2z_0^2 - \rho^2}{(|\vec{\rho}|^2 + z_0^2)^{\frac{5}{2}}} \right) J_0(k\rho) \rho d\rho = \frac{\mu_0 m}{2} k e^{-kz_0}$$

In Fourier-Bessel (Hankel) space, a 2D Gaussian in the form of

$$g(\rho) = e^{-\frac{\rho^2}{2\sigma^2}}$$

can be represented as

$$\tilde{g}(k) = \int_0^\infty e^{-\frac{\rho^2}{2\sigma^2}} J_0(k\rho) \rho d\rho = \sigma^2 e^{-\frac{1}{2}\sigma^2 k^2}$$

Through numerically evaluating the physics-derived transformed field along with the transformed Gaussian, we found that the two functions match at mid frequency range (k between 1-10), consistent with the sampling regime with low resolution at high frequency (limited by the sensor grid density) and small sampling range and low frequency (limited by the small geometrical footprint of the sensor patch).

Thus, Gaussians provide physically motivated and computationally efficient surrogates for the magnetic-field distributions of individual small dipole sources.

The first step of the PAGO-DeMag algorithm is to normalize the raw sensor data from the 8 × 8 Hall effect sensor array and interpolate the low-res sensor data into a 20 × 20 mid-res image.

$$I \in \mathbb{R}^{8\times 8}$$

$$U = \mathrm{resize}(I,\ \mathrm{shape} = (20 \times 20), \mathrm{method} = \mathrm{'linear'})$$

$$U \leftarrow \frac{U}{\max(U)}$$

After interpolation, we conducted iterative Gaussian inhibition. That is, we detected the primary peak and inhibited the peak with a Gaussian mask. This process is iterated to find all peaks until the next peak has a height smaller than a set threshold to provide initial guesses for the xy positions for next step:

$$(p_k,\ q_k) = \underset{(x,y)}{\mathrm{argmax}}(N_{k-1}[x,y])$$

$$G_k[x,y] = \exp(-\frac{(x-p_k)^2 + (y-q_k)^2}{2\sigma^2})$$

$$M_k = 1 - G_k$$

$$N_k = M_k \circ U$$

After the initial guesses have been generated through iterative inhibition, the position prediction then becomes an optimization problem: optimizing the linear combinations of Gaussians (acting as strong priors) to minimize the mean-squared error relative to the interpolated image, starting from initial guesses using the limited-memory Broyden–Fletcher–Goldfarb–Shanno (L-BFGS) algorithm, which is computationally efficient for multivariable optimization and suitable for real-time applications.

$$\widehat{U}[x,y;\theta] = \sum_{k=1}^{n} \alpha_k \cdot \exp(-\frac{(x-x_k)^2 + (y-y_k)^2}{2\sigma^2})$$

$$\mathcal{L}[\theta] = \sum_{x=1}^{20}\sum_{y=1}^{20}\left(U[x,y] - \widehat{U}[x,y,\theta]\right)^2, \qquad \theta^* = \underset{\theta}{\mathrm{argmin}}(\mathcal{L}[\theta])$$

Following prediction of the xy-position, we predict the height by multiplying the square root of height of the Gaussian optimized in the previous step (α_k) with an experimentally determined calibration factor describing the empirical relationship between fitted Gaussian amplitude and source–sensor distance:

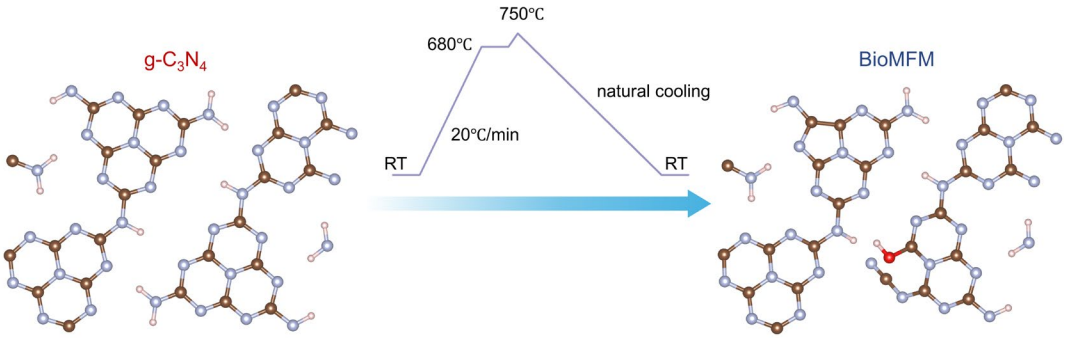
$$H_k = h \cdot \frac{1}{\sqrt{\alpha_k}}$$

PAGO-DeMag circumvents localized corrupted sensor data by projecting the discrete Hall array inputs onto a continuous linear combination of spatially smooth Gaussian basis functions (**Supplementary Figure 35**). Mathematically, any localized hardware perturbation $\delta B(x,y)$ is filtered through an integral overlap with the continuous basis functions:

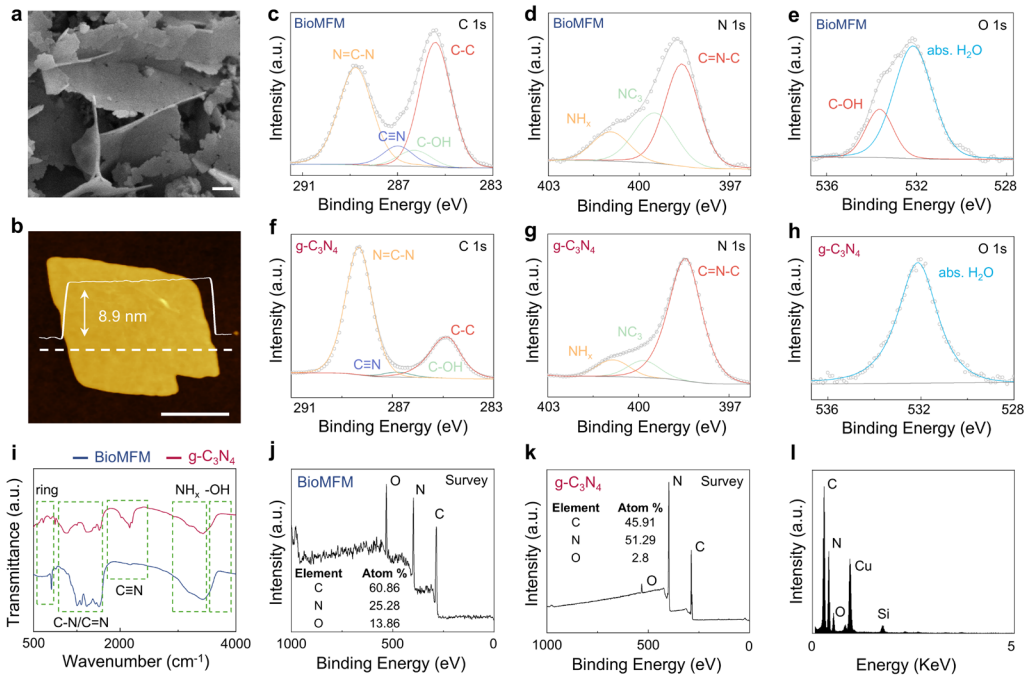
$$\alpha_i = \iint [B_{real}(x,y) + \delta B(x,y)] \cdot \exp\left(-\frac{(x-x_i)^2 + (y-y_i)^2}{2\sigma_i^2}\right) dxdy$$

where α_i represents the linear combination weight of the i-th basis function; x_i, y_i define the geometric center coordinates of the i-th basis function mapped onto the Hall sensor array plane; and σ_i governs the feature decay width of the Gaussian profile.

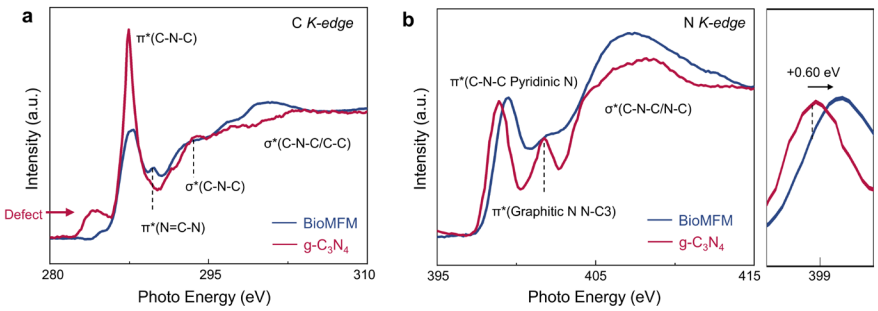
Within this framework, each parameterized basis function is uniquely and completely defined by the parameter vector $\{\alpha_i, x_i, y_i, \sigma_i\}$, mapping specific micro-scale and macro-scale physical dimensions of the bioelectronic interface.



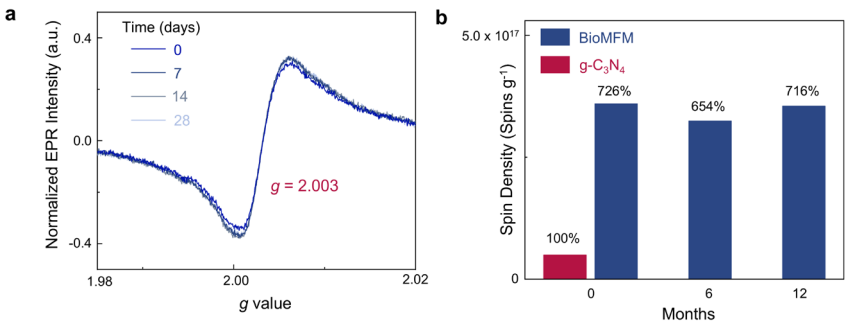
Supplementary Figure 1 Controlled thermal synthesis and structural evolution of BioMFM. Schematic illustrating the metal-free transformation of pristine g-C_3N_4 (left) into ferromagnetic BioMFM (right). The temperature–time profile (middle) depicts a heating ramp of 20 °C/min with a primary annealing stage at 680 °C followed by a rapid thermal excursion to 750 °C. This sequential thermal treatment facilitates selective C-N bond cleavage (de-nitrogenation) while preserving the core heptazine ring integrity. The subsequent structural reconstruction yields unsaturated C/N sites bearing itinerant 2p electrons, establishing an extended π–σ conjugated framework populated with C–C• and -C≡N motifs. The synthesis is conducted without metal catalysts or precursors, ensuring a purely organic composition of C, N, and O that underpins the emergent metal-free ferromagnetism.



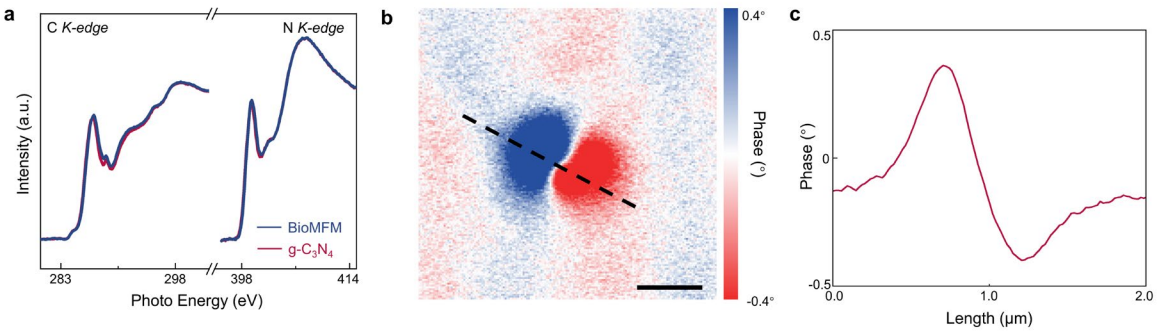
Supplementary Figure 2 Morphological and compositional characterization of BioMFM and precursor g-C_3N_4. **a** SEM micrograph of BioMFM flakes, showing a typical layered morphology (scale bar, 200 nm). **b** AFM topographic image and height profile of a representative BioMFM flake with a thickness of ~8.9 nm (scale bar, 1 μm). **c–e** High-resolution XPS spectra of BioMFM: **c** C 1s deconvolution showing N=C–N (sp^2), C–C, and C–OH components; **d** N 1s deconvolution into NC_3/C–N=C and $–NH_x$ species; **e** O 1s deconvolution dominated by C–OH and adsorbed H_2O. **f–h** Corresponding **f** C 1s, **g** N 1s, and **h** O 1s spectra for g-C_3N_4, serving as a baseline for the stoichiometric framework. **i** FTIR spectra of BioMFM and g-C_3N_4 showing retained heptazine ring signatures (C–N stretching at 1200–1650 cm^{-1}; tri-s-triazine breathing near ~810 cm^{-1}), while the emergent C≡N vibrations in BioMFM confirm framework reconstruction. **j, k** XPS survey spectra and derived atomic compositions confirming a metal-free framework, with a total absence of any identifiable transition-metal core-level signatures. **j** BioMFM (C: 60.86 at%, N: 25.28 at%, O: 13.86 at%) versus **k** g-C_3N_4 (C: 45.91 at%, N: 51.29 at%, O: 2.8 at%). The significantly elevated C/N ratio in BioMFM provides quantitative evidence for the de-nitrogenation mechanism. **l** EDS spectrum corroborating the purely organic composition (C, N, O); the Cu signal originates from the supporting TEM grid and the trace Si signal represents non-magnetic environmental residuals. Three experiments in **a** and **b** were repeated independently with similar results.



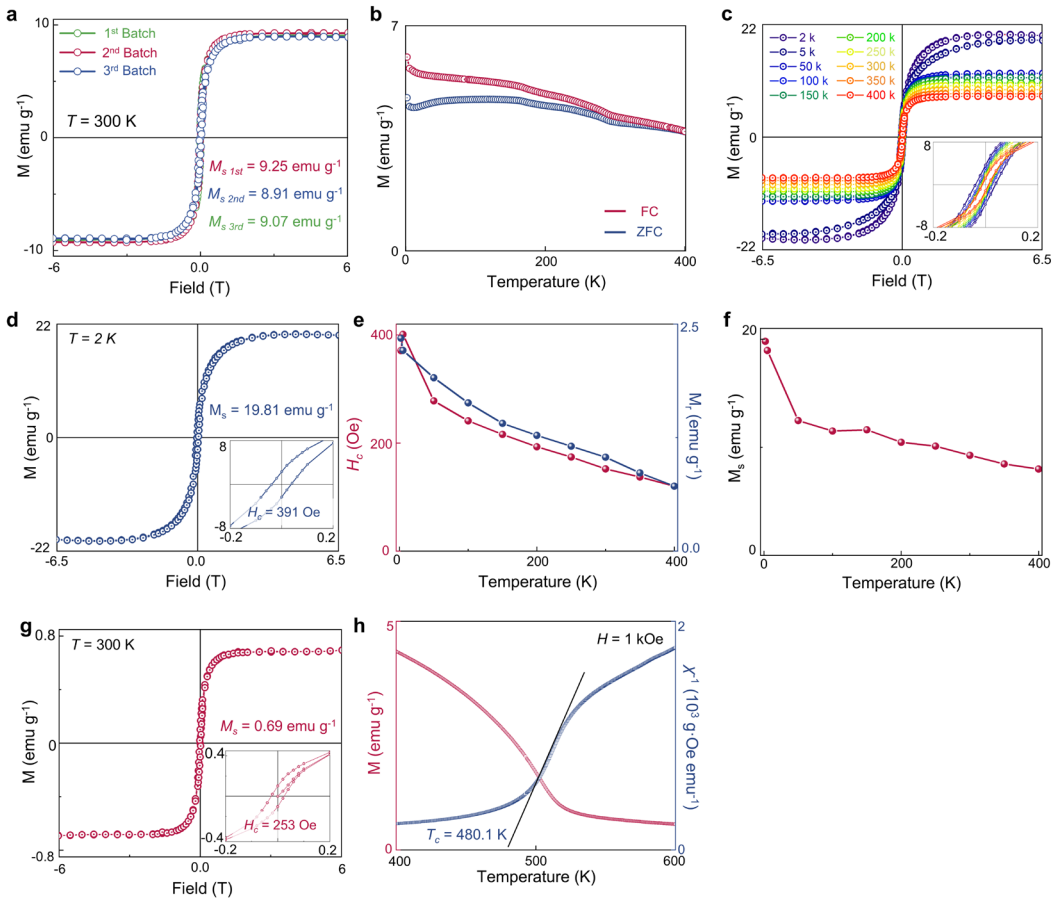
Supplementary Figure 3 Synchrotron XANES spectra resolving element-specific electronic structure and framework reconstruction. a C K-edge XANES of BioMFM and g-C_3N_4, showing redistributed π* resonances and an enhanced defect-associated pre-edge feature in BioMFM, signifying structural reconstruction. **b** N K-edge XANES revealing a prominent peak shift of + 0.60 eV and modifications in the NC_3/C–N=C manifold, consistent with the de-nitrogenation mechanism.



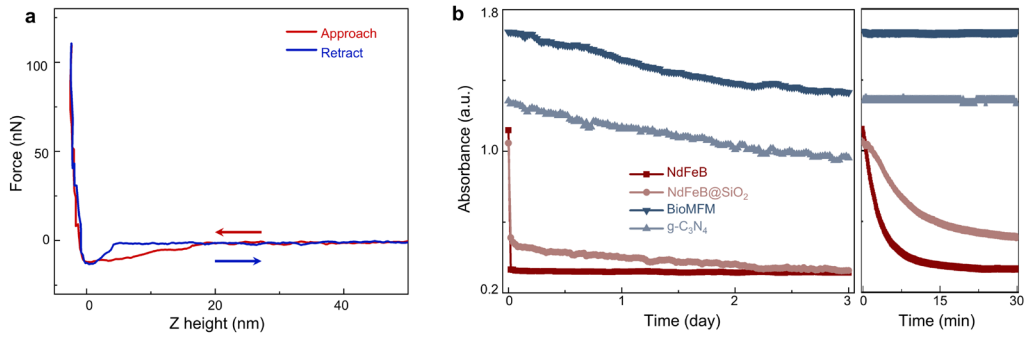
Supplementary Figure 4 Longitudinal EPR tracking and ambient stability of framework radical centers. a High-resolution ambient EPR spectra recorded continuously over a 28-day open-air exposure timeline, exhibiting pristine retention of lineshape symmetry and a stable Landé factor at g = 2.003. **b** Quantitative tracking of bulk spin density over an extended 12-month ambient aging window relative to pristine g-C_3N_4 controls, demonstrating the long-term stability of defect-associated radical states under ambient conditions.



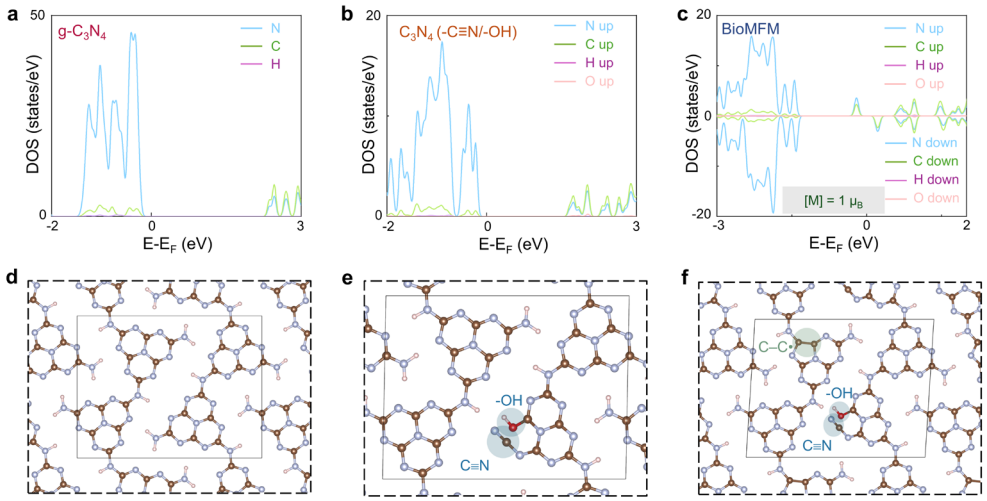
Supplementary Figure 5 Element-specific spin polarization and magnetic domain configurations of BioMFM. a Field-reversal XAS at ±1 T exhibiting a clear reversible asymmetry (XMCD-like response), providing direct evidence of spin polarization at the light-element (C/N) edges. **b** MFM phase image of BioMFM displaying robust dipolar magnetic contrast from localized domains (scale bar, 1 μm). **c** MFM phase profile along the cross-sectional path indicated in **b**, confirming nanoscale magnetic contrast with a significant phase shift (~±0.4°).



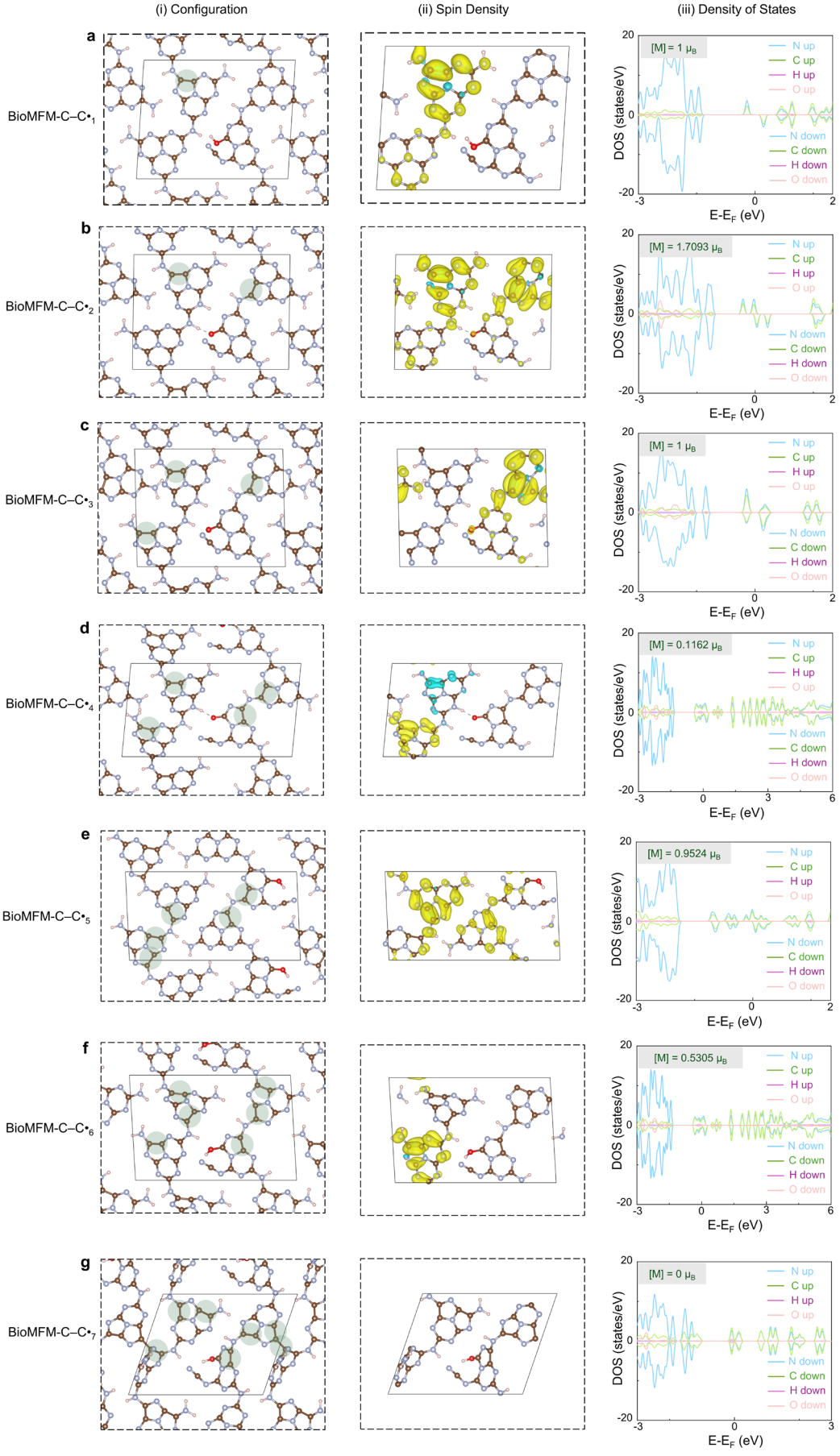
Supplementary Figure 6 Macroscopic magnetometry, synthetic reproducibility, and high-temperature ferromagnetic phase transitions of BioMFM. a Field-dependent magnetization (M-H) hysteresis loops recorded at 300 K across three independent, chronological synthesis batches manufactured under identical rapid thermal annealing parameters, demonstrating robust processing control and structural reliability. **b** Zero-field-cooled (ZFC) and field-cooled (FC) magnetization vs. temperature curves recorded from 2-400 K. The pronounced bifurcation between ZFC and FC branches at low temperatures is indicative of robust spontaneous magnetic ordering. **c** Isothermal M-H hysteresis loops recorded across a range of temperatures from 2-400 K, demonstrating persistent ferromagnetism across the entire biological and ambient temperature range. **d** Detailed M-H loop at 2 K showing a saturation magnetization (M_s) of 19.81 emu g^{-1} and enhanced coercivity H_c = 391 Oe. **e** Temperature dependence of H_c and remanence (M_r) showing a monotonic decrease consistent with increased thermal agitation and domain-wall softening upon warming. **f** Temperature dependence of M_s, confirming the stability of the ferromagnetic phase well above physiological temperatures. **g** Room-temperature (300 K) M-H loop for the 10 wt% BioMFM-PNIPAM composite hydrogel, showing retention of a ferromagnetic hysteresis response after incorporation into the PNIPAM matrix. **h** The intersection of the magnetization M(T) and inverse susceptibility $\chi^{-1}(T)$ curves at T_c = 480.1 K confirms an above-room-temperature ferromagnetic transition. Temperature-dependent magnetometry further establishes the robustness of the ferromagnetic state beyond ambient conditions.



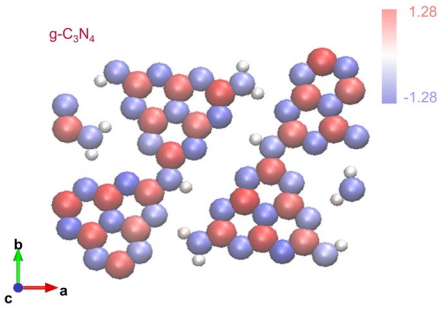
Supplementary Figure 7 Nanomechanical profiling and long-term colloidal stability tracking of BioMFM. a Representative AFM force–distance curves capturing the precise tip–sample approach (red trace) and retract (blue trace) trajectories. Quantitative extraction via the Johnson–Kendall–Roberts (JKR) contact mechanics model establishes a compliant Young's modulus of ~3.44 GPa, balancing high intralayer integrity with flexible interlayer sliding. **b** Time-course UV-vis absorbance retention profiles monitored at a wavelength of 400 nm over an extended 3-day tracking matrix (left panel) and an initial 30-minute immediate window (right panel). The trajectories demonstrate that BioMFM effectively resists gravitational sedimentation and dipole-induced macro-aggregation, matching the pristine colloidal stability of metal-free g-C_3N_4 frameworks while vastly outperforming inorganic metallic controls, bare NdFeB, and NdFeB@SiO_2.



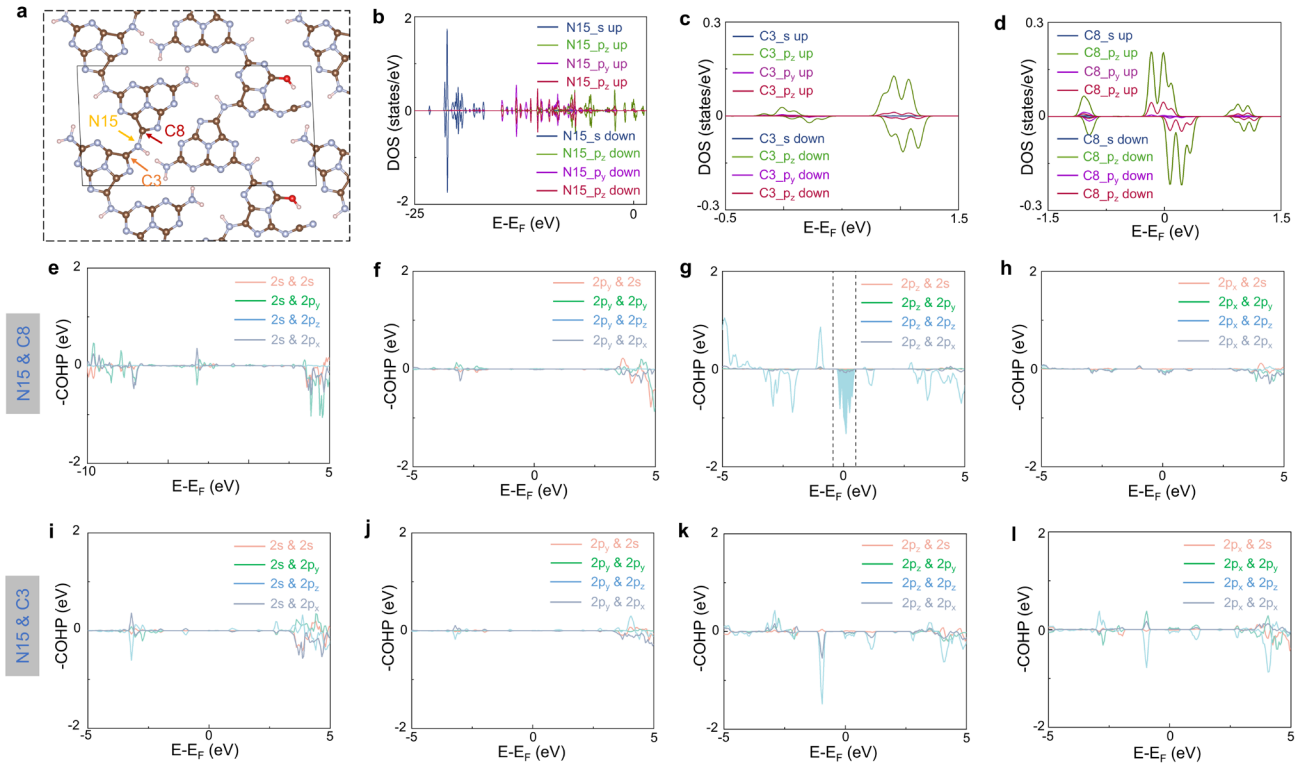
Supplementary Figure 8 Theoretical electronic structures and relaxed atomic configurations of g-C_3N_4 derivatives. a Spin-resolved density of states (DOS) for pristine g-C_3N_4, exhibiting a non-magnetic ground state with fully compensated spin channels. **b** DOS for surface-functionalized C_3N_4 containing –C≡N and –OH terminations without de-nitrogenation; the framework remains spin-compensated, indicating that surface functionalization alone is insufficient to induce spontaneous magnetization. **c** DOS for a BioMFM model featuring a single de-nitrogenation-induced C-C• radical center. The electronic structure exhibits pronounced exchange splitting at the Fermi level (E_F = 0 eV) and a net magnetic moment of ~1 μ_B, with spin polarization primarily dominated by C/N 2p states. **d–f** Relaxed atomic structures corresponding to the electronic configurations in **a–c**: **d** pristine g-C_3N_4, **e** functionalized g-C_3N_4, **f** BioMFM. Brown, blue, red, and white spheres denote C, N, O, and H atoms, respectively; the active C-C• spin center in **f** is highlighted (green).


(i) Configuration
(ii) Spin Density
(iii) Density of States
a
BioMFM-C–C•1
[M] = 1 μB
b
BioMFM-C–C•2
[M] = 1.7093 μB
c
BioMFM-C–C•3
[M] = 1 μB
d
BioMFM-C–C•4
[M] = 0.1162 μB
e
BioMFM-C–C•5
[M] = 0.9524 μB
f
BioMFM-C–C•6
[M] = 0.5305 μB
g
BioMFM-C–C•7
[M] = 0 μB
N up
C up
H up
O up
N down
C down
H down
O down
DOS (states/eV)
E-EF (eV)

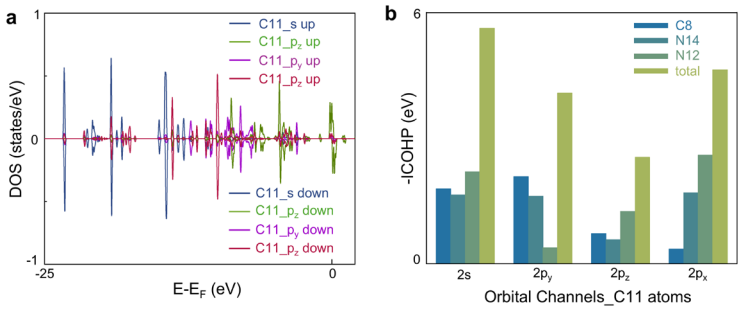
Supplementary Figure 9 Evolution of electronic structure and magnetic moments with increasing C-C• concentration. Spin-polarized DFT calculations illustrating the dependence of ferromagnetism on the multiplicity of de-nitrogenation-induced C-C• radical centers. **a–g** Comparative analysis for BioMFM-C-C•$_x$ (x = 1–7), with each row depicting: **(i)** Configuration: Relaxed atomic structures with C-C• sites highlighted (green circles); **(ii)** Spin Density: 3D spin-polarization density isosurfaces, where yellow lobes denote majority-spin and cyan/blue lobes denote minority-spin density; and **(iii)** Density of States: Atom-projected, spin-resolved DOS referenced to the Fermi level (E_F = 0 eV). The total magnetic moment (|M|) for each configuration is annotated: 1, 1.7093, 1, 0.1162, 0.9524, 0.5305, and 0 μ_B for x = 1-7, respectively. Increasing radical concentration initially introduces defect states near E_F that break spin degeneracy and foster long-range order. However, the magnitude of |M| follows a non-monotonic trend governed by both the spatial distribution and geometric coupling of the radical sites. For the x = 7 configuration examined here, pronounced structural distortion quenches the net moment, indicating that specific high-defect configurations can disrupt the underlying π-network and suppress magnetic order.



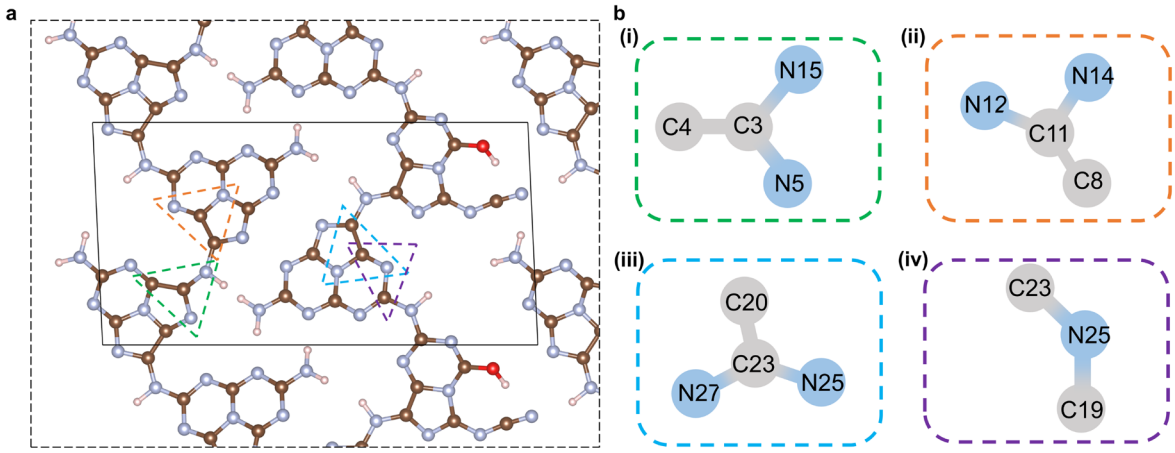
Supplementary Figure 10 Bader charge distribution of the pristine g-C_3N_4. Bader charge analysis[4] obtained from spin-polarized DFT calculations, serving as a stoichiometric baseline for evaluating defect-induced electron redistribution in BioMFM. Pristine g-C_3N_4 exhibits pronounced charge localization within the heptazine network, characterized by strong C-N polarity and significant charge separation prior to de-nitrogenation. This localized electronic state stands in contrast to the enhanced delocalization and reduced polarity observed upon the formation of the π–σ conjugated framework in BioMFM. Atom spheres are colored by Bader charge Δq: blue denotes charge gain, red denotes charge loss (color-bar ranges as shown for each panel).



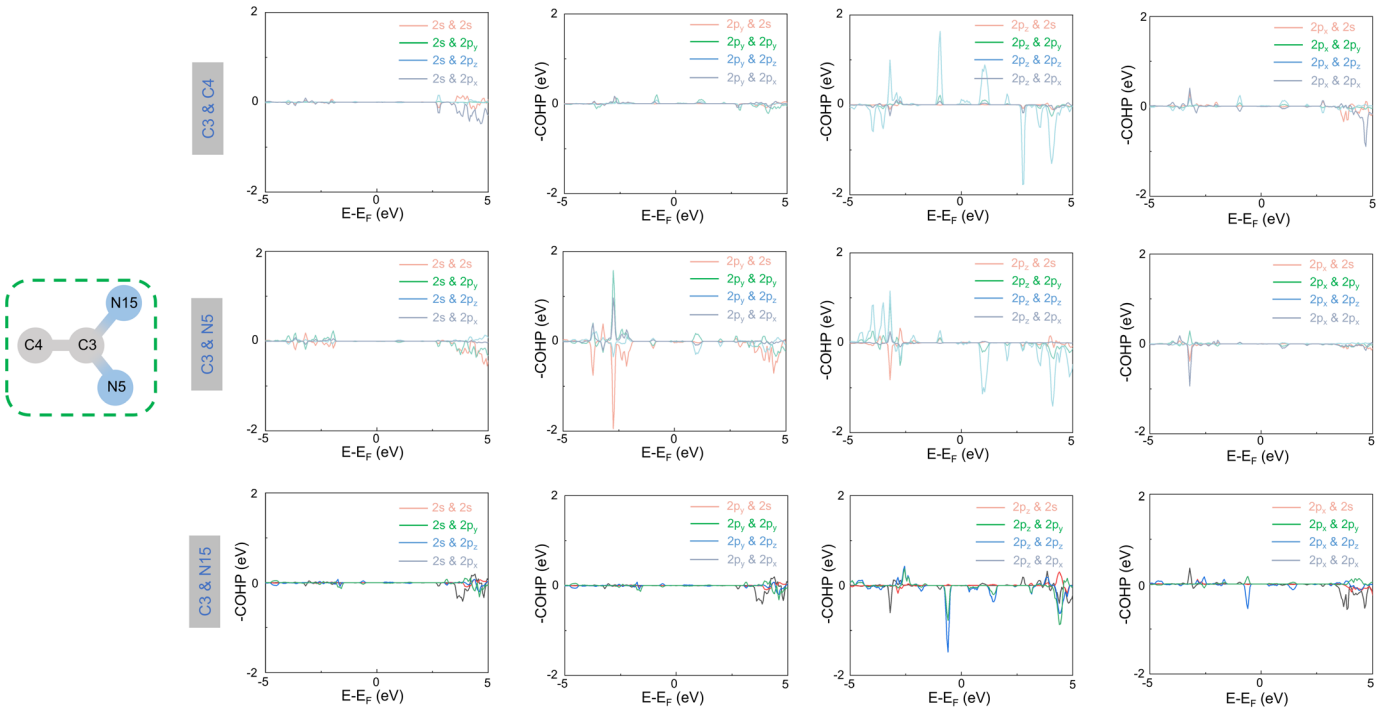
Supplementary Figure 11 Orbital-resolved electronic structure and bonding stabilization in the C-C• defect region. a Relaxed atomic structure of BioMFM-C-C•$_1$, identifying the representative nitrogen (N15) and carbon (C3, C8) sites used for localized electronic analysis. **b–d** Site- and spin-resolved projected density of states (PDOS) for **b** N15, **c** C3, and **d** C8 relative to the Fermi level (E_F = 0 eV). N15 exhibits a pronounced P_z weight spanning E_F, while the carbon sites show significant spin-splitting, collectively signifying defect-localized spin polarization. **e–h** Orbital-decomposed Crystal Orbital Hamilton Population (COHP) for the N15-C8 bond across the s, P_y, P_z, and P_x channels. The P_z channel contributes the weakest bonding stabilization and retains significant antibonding weight near E_F. **i–l** COHP analysis for the N15-C3 bond, likewise revealing a prominent P_z antibonding population crossing E_F and reduced bonding strength relative to the in-plane (P_x, P_y) channels. Results are plotted in the -COHP convention, where values >0 indicate bonding and values <0 indicate antibonding states; spin-up and spin-down channels are shown separately. Collectively, these results demonstrate that de-nitrogenation generates itinerant P_z-dominated antibonding states at E_F, facilitating the exchange splitting required to stabilize the ferromagnetic ground state in BioMFM.



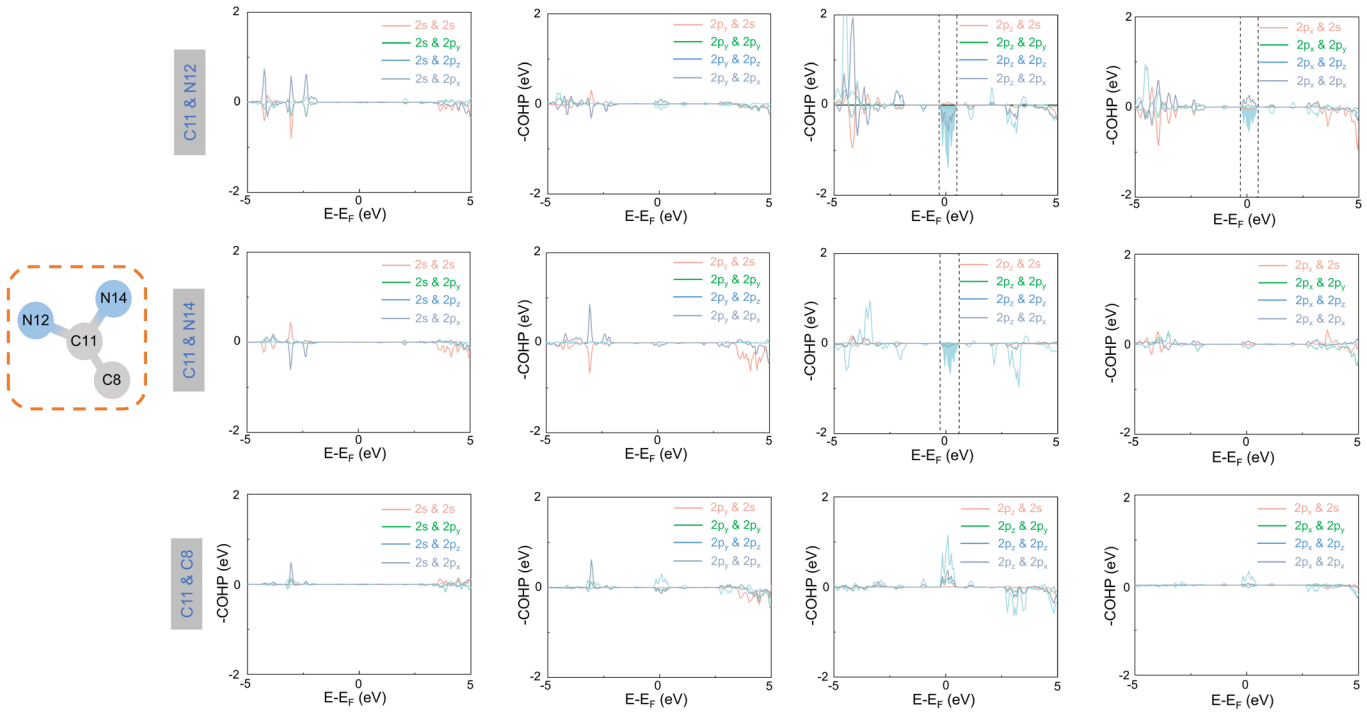
Supplementary Figure 12 Site-specific electronic states and orbital-resolved bonding stabilization at the C-C• defect. a Spin-polarized, orbital-resolved PDOS for the C11 atom adjacent to the de-nitrogenation-induced defect. The spectrum reveals pronounced spin-split P_z states straddling the Fermi level (E_F = 0 eV), confirming the primary participation of out-of-plane 2p orbitals in the emergent magnetic state. **b** Integrated −ICOHP for C11-C8, C11-N14, and C11-N12 bonds, decomposed by orbital channel (s, P_x, P_y, P_z). In the −COHP convention, larger positive values indicate stronger bonding stabilization; across all analyzed bonds, the P_z channel contributes the smallest −ICOHP magnitude, whereas s, P_x, and P_y channels dominate the framework's bonding strength. This systematically weaker P_z bonding facilitates the retention of partially unpaired itinerant 2p electrons on the reconstructed π–σ framework, thereby enabling the exchange splitting required to stabilize the ferromagnetic ground state.



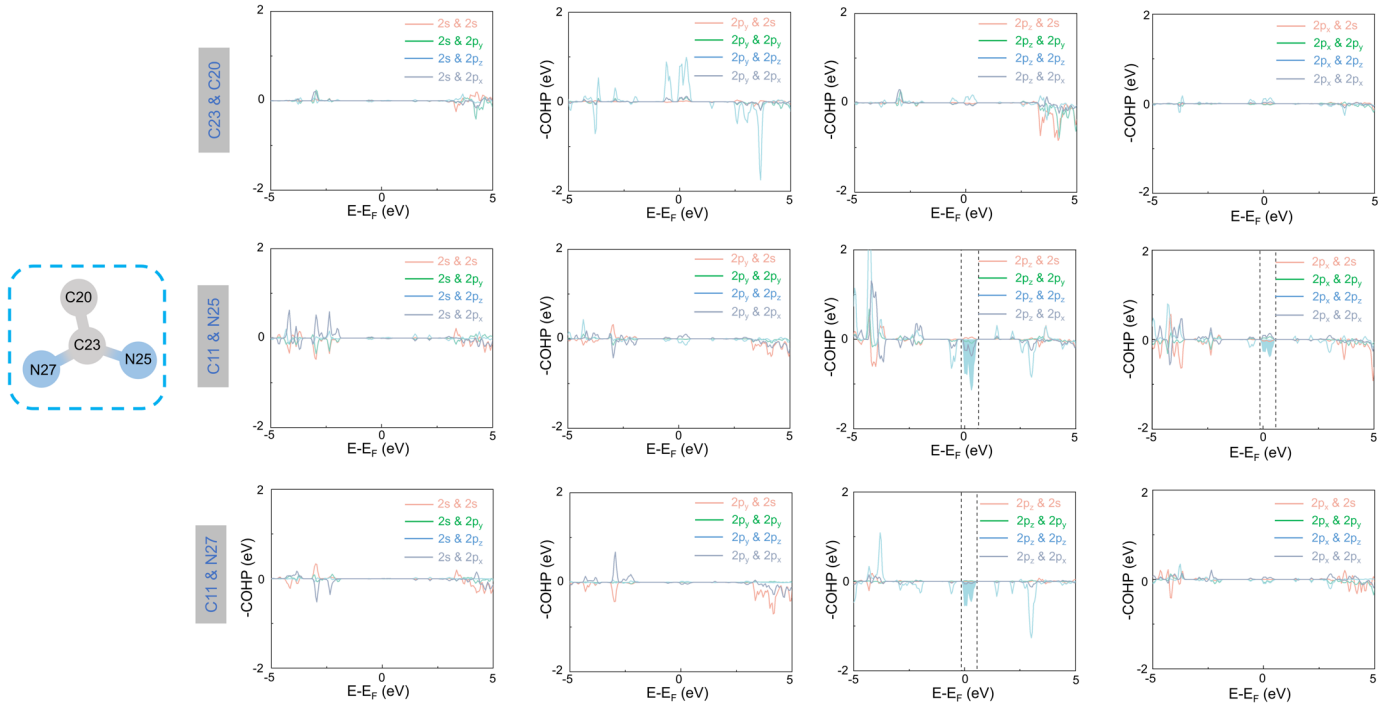
Supplementary Figure 13 Local bonding motifs and nearest-neighbor environments in the BioMFM-C-C•$_4$. a Relaxed atomic structure of a BioMFM supercell featuring four de-nitrogenation-induced C-C• radical centers. Colored dashed triangles identify the four inequivalent probe sites selected for detailed bond-resolved analysis: C3 (green), C11 (orange), C23 (blue), N25 (purple). **b** Magnified schematics of the first-shell coordination environments for each probe site: **(i)** C3-C4/N5/N15, **(ii)** C11-N12/N14/C8, **(iii)** C23-N25/N27/C20, **(iv)** N25-C23/C19. These representative motifs were utilized for COHP calculations to quantify the orbital-specific antibonding weight near the Fermi level, elucidating how local geometric distortions in the reconstructed π–σ framework stabilize long-range ferromagnetic order.



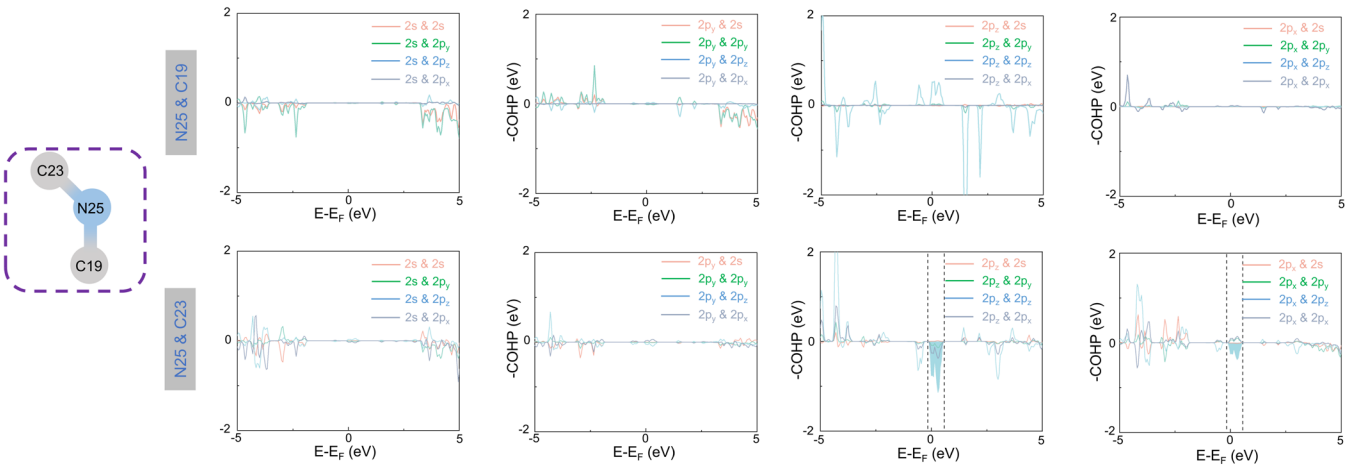
Supplementary Figure 14 Orbital-resolved bonding analysis and electronic states at the C3 site. Orbital-decomposed −COHP curves for C3-C4 (top), C3-N5 (middle), and C3-N15 (bottom) bonds in the BioMFM-C-C•$_4$ supercell. Analysis is performed across the s, P_x, P_y, and P_z orbital channels, with spin-up and spin-down components resolved separately relative to the Fermi level (E_F = 0 eV). In the -COHP convention, values > 0 denote bonding and values < 0 denote antibonding states. While σ-type channels exhibit strong bonding stabilization well below E_F, the out-of-plane P_z channel is systematically weaker and retains a prominent antibonding weight near E_F, most evident in the C3-N15 interaction. These results establish that the C3 site hosts itinerant P_z-dominated antibonding states at the valence-band edge, favoring the exchange splitting required to stabilize the ferromagnetic ground state in BioMFM.



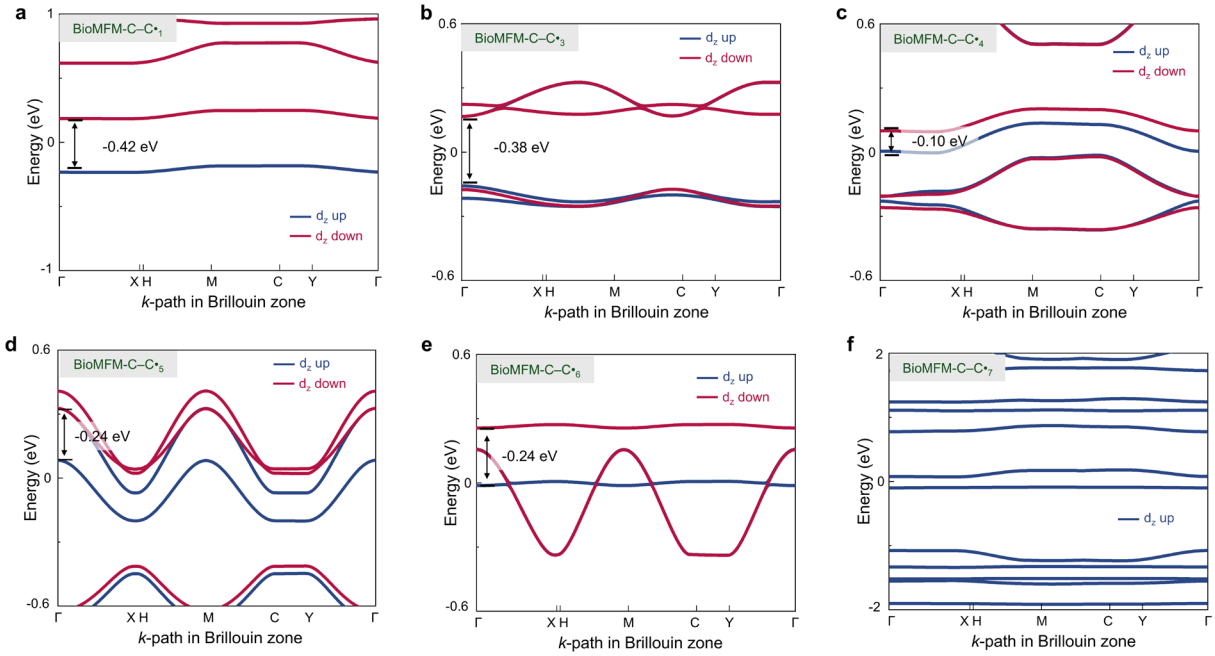
Supplementary Figure 15 Orbital-resolved bonding analysis and electronic states at the C11 site. Orbital-decomposed −COHP curves for C11–N12 (top), C11–N14 (middle), and C11–C8 (bottom) bonds in the BioMFM-C-C•$_4$ supercell. Analysis is performed relative to the Fermi level (E_F = 0 eV), with spin-up and spin-down components resolved separately across the s, P_x, P_y, and P_z channels. While σ-type channels remain strongly bonding well below E_F, the out-of-plane P_z channel is systematically weakest and exhibits a prominent antibonding weight near E_F, most evident for the C11-N14 bond. By contrast, the C11-C8 bond retains comparatively higher σ bonding stabilization. These findings demonstrate that defect-adjacent C-N bonds undergo selective weakening in the P_z channel, facilitating the retention of partially unpaired itinerant P_z electrons that drive localized spin polarization and stabilize the ferromagnetic ground state in BioMFM.



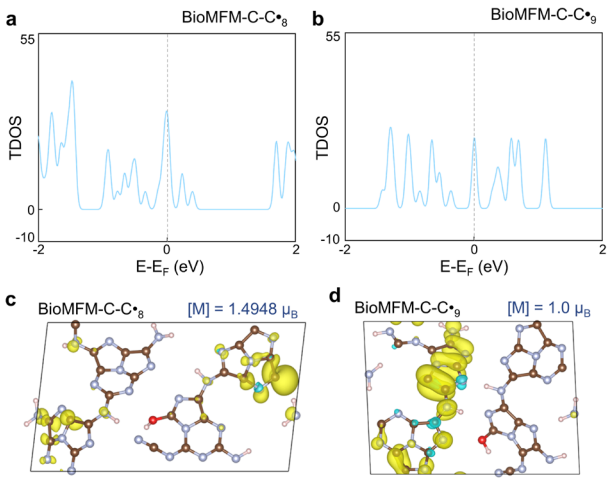
Supplementary Figure 16 Orbital-resolved bonding analysis and electronic states at the C23 site. Orbital-decomposed −COHP curves for C23–C20 (top), C23–N25 (middle), and C23–N27 (bottom) in the BioMFM-C-C•$_4$ supercell. Calculations resolve contributions from the s, P_x, P_y, and P_z channels relative to the Fermi level (E_F = 0 eV), with spin-up and spin-down components shown separately. The C23-C20 bond exhibits robust σ bonding stabilization well below E_F with minimal P_z orbital weight near the valence-band edge. In contrast, the C23-N25 and C23-N27 motifs display pronounced P_z antibonding weight surrounding E_F, while their respective σ channels remain deeply bonding. These findings establish that C23 acts as a structural conduit, facilitating the delocalization of itinerant P_z spin polarization from the defect center into neighboring heptazine rings. The strong near-E_F antibonding character, particularly in the C23-N25 bond, favors the exchange-driven stabilization required for maintaining long-range ferromagnetic order across the π–σ conjugated framework.



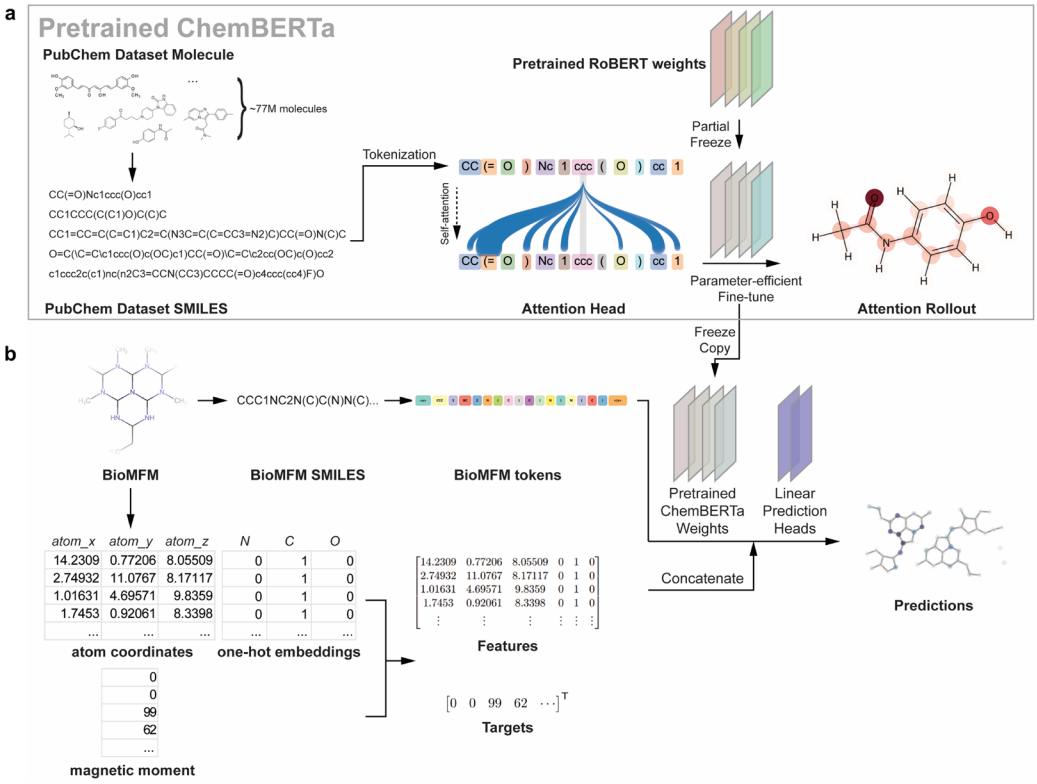
Supplementary Figure 17 Orbital-resolved bonding analysis and electronic states at the N25 site. Orbital-decomposed −COHP curves for N25-C19 (top) and N25-C23 (bottom) in the BioMFM-C-C•$_4$ supercell. Calculations resolve contributions from the s, P_x, P_y, and P_z channels relative to the Fermi level (E_F = 0 eV), with spin-up and spin-down components shown separately. The N25-C19 bond is dominated by robust σ bonding stabilization at lower energy levels, with minimal P_z orbital weight near the valence-band edge. Conversely, the N25-C23 interaction demonstrates pronounced P_z antibonding weight surrounding E_F, while its respective σ channels exhibit reduced bonding strength compared to the N25-C19 motif. These findings reveal that N25 serves as a critical structural junction within the de-nitrogenation-driven P_z spin network, enabling the long-range transmission of localized spin polarization across the reconstructed π–σ conjugated framework. The high occupancy of itinerant P_z-dominated antibonding states at E_F facilitates the exchange splitting required to stabilize the ferromagnetic ground state in BioMFM.



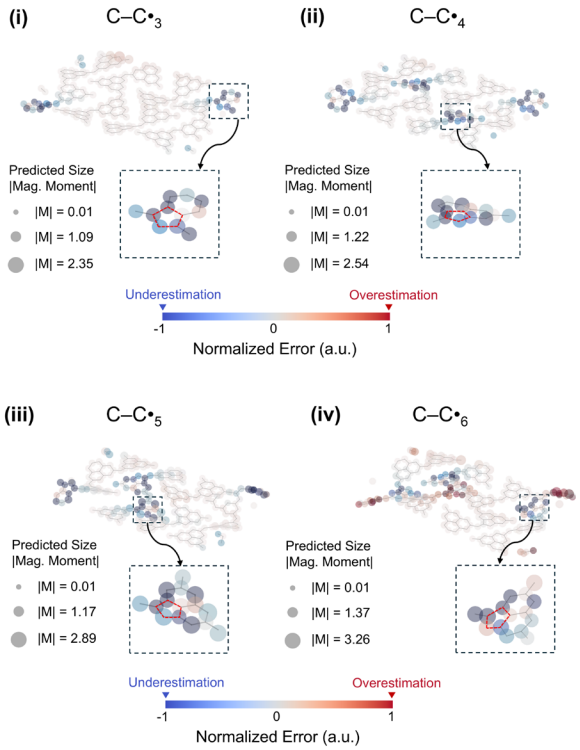
Supplementary Figure 18 Evolution of spin-polarized electronic band structures with increasing C-C• multiplicity. Spin-polarized DFT band structures computed along the high-symmetry k-path of the supercell Brillouin zone for BioMFM-C-C•$_x$: **a** x = 1, **b** x = 3, **c** x = 4, **d** x = 5, **e** x = 6, and **f** x = 7 (energies referenced to the Fermi level, E_F = 0 eV). Blue and red curves represent the spin-up and spin-down channels, respectively. Pronounced exchange splitting is observed in the bands crossing E_F for x = 1-6, with representative magnitudes (|ΔE|) of **a** ~0.42 eV, **b** ~0.38 eV, **c** ~0.10 eV, **d** ~0.24 eV, and **e** ~0.24 eV. The coexistence of a finite density of states at E_F [$N(E_F)$] and significant exchange splitting satisfies the *Stoner* criterion (S > 1), confirming the itinerant ferromagnetic ground state in BioMFM. Conversely, for **f** x = 7, the near-degenerate bands at E_F indicate quenched spin polarization, demonstrating that excessive de-nitrogenation disrupts the π–σ conjugated framework and suppresses long-range magnetic order.



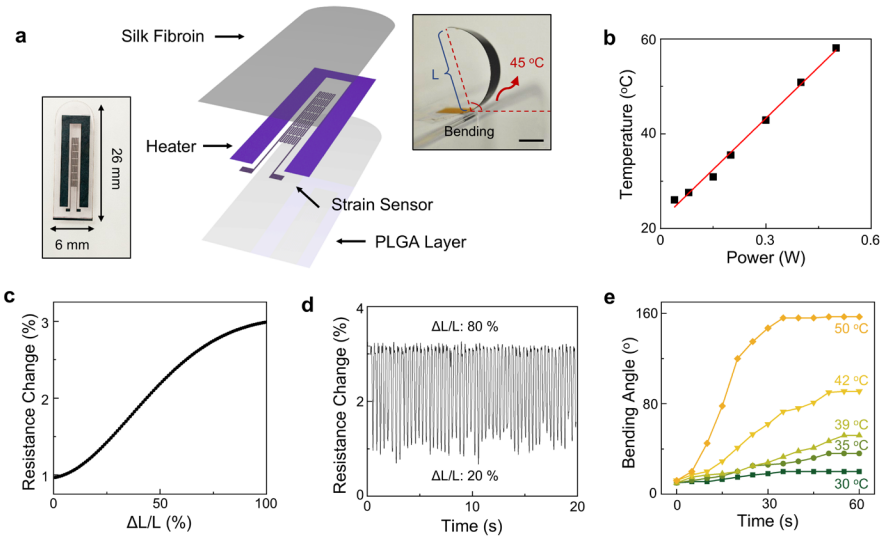
Supplementary Figure 19 Spin-unpolarized density of states and spatial spin-density distributions for high-density C-C• configurations. a, b Spin-unpolarized TDOS of **a** BioMFM-C-C•$_8$ and **b** BioMFM-C-C•$_9$, showing pronounced near-Fermi DOS features that persist across E_F. **c, d** Corresponding real-space spin density isosurface configurations for **c** x = 8 and **d** x = 9, confirming that the intrinsic ferromagnetism consistently obeys a unified *Stoner* splitting model over an extended radical concentration regime.



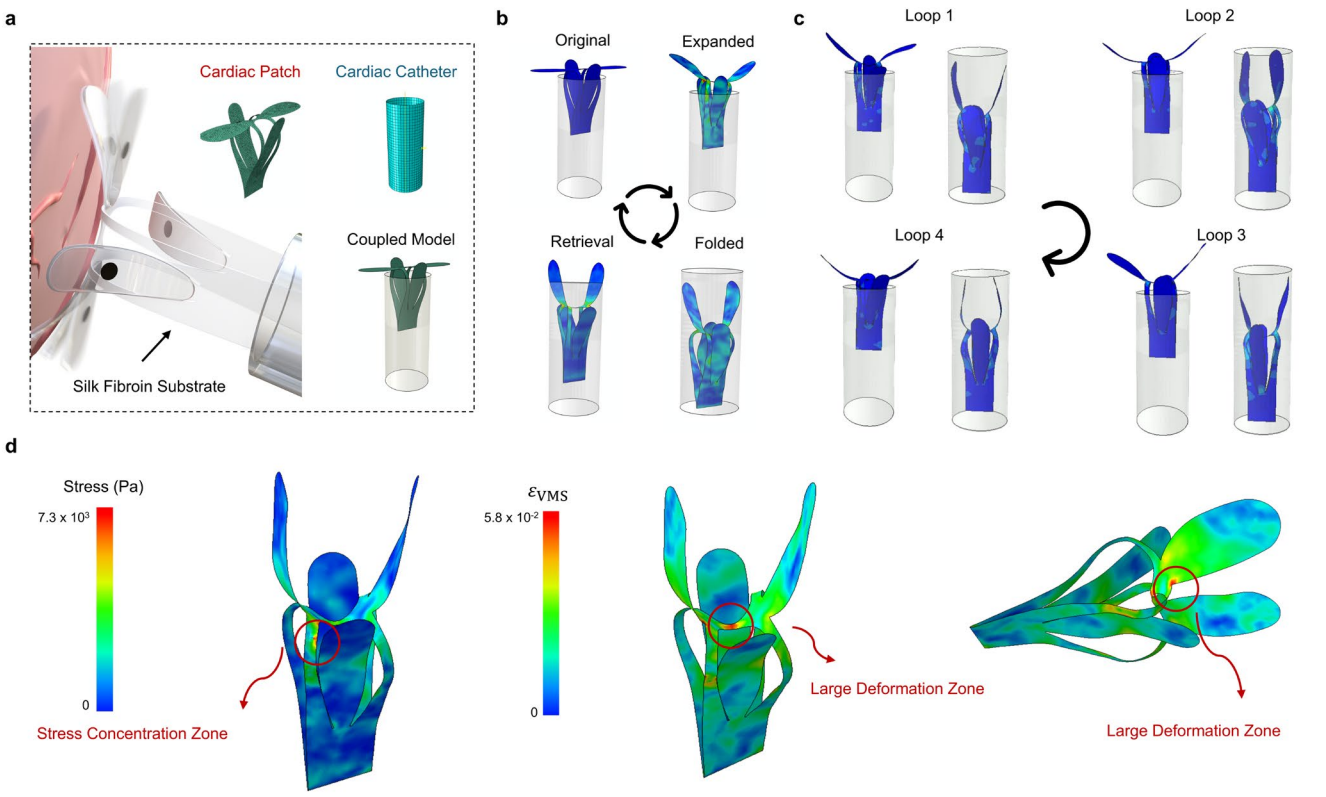
Supplementary Figure 20 Architecture and implementation of the FT-ChemBERTa model for atom-resolved magnetic moment prediction. a Pretrained ChemBERTa[3] was first derived from a RoBERTa transformer trained on ~77 million PubChem molecules, in which SMILES strings were tokenized and passed through self-attention layers to learn contextual chemical representations; attention rollout visualizations highlighted chemically relevant substructures associated with spin density (top). During downstream use, these pretrained weights were partially frozen for parameter-efficient fine-tuning. For BioMFM, each molecule was represented both as a SMILES string and as an array of atomic descriptors comprising 3D Cartesian coordinates and one-hot elemental identity (C, N, O). **b** BioMFM SMILES were tokenized and embedded by the frozen ChemBERTa encoder to provide a global molecular context, while atomic descriptor matrices supplied local geometric information (bottom). The molecular embeddings and atomic features were concatenated and passed to learnable linear prediction heads to regress per-atom magnetic moments, using DFT-derived atomic moments as training targets. This hybrid chemical-language/geometry model produced atom-resolved magnetic-moment predictions that could be mapped back onto the BioMFM structure for comparison with DFT calculations and visualization of error distributions.



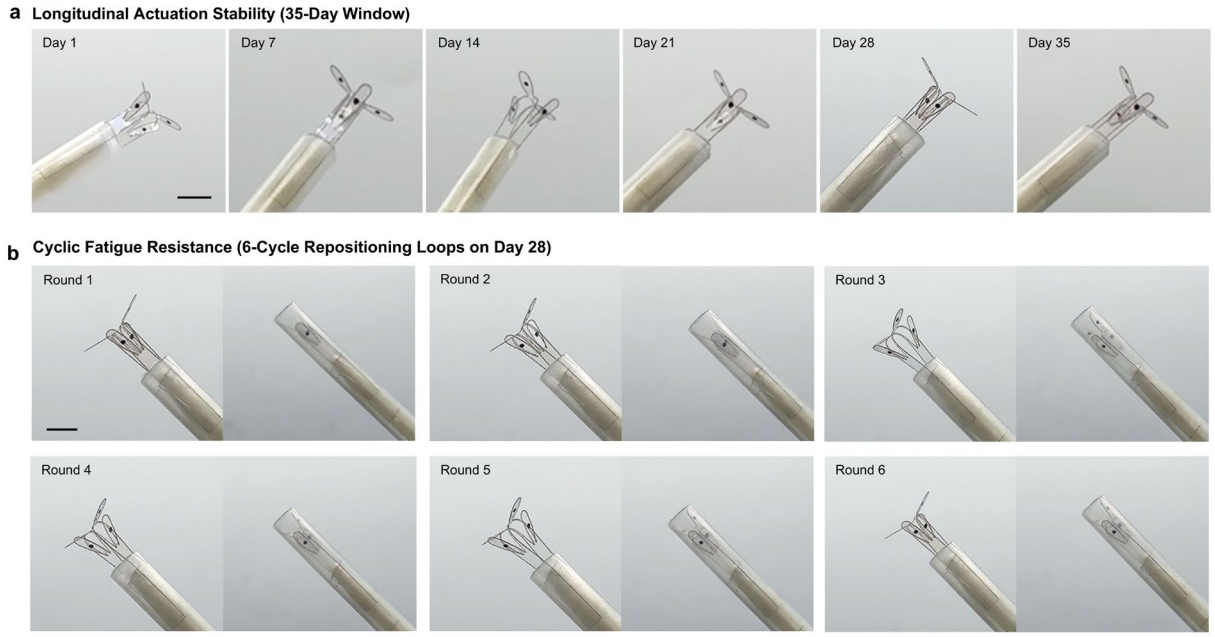
Supplementary Figure 21 Spatial error distribution and interpretability of FT-ChemBERTa magnetic moment predictions. Spatial comparison between fine-tuned ChemBERTa (FT-ChemBERTa) and DFT reference magnetic moments for four representative BioMFM-C-C•$_x$ molecules: **(i)** C–C•$_3$, **(ii)** C-C•$_4$, **(iii)** C-C•$_5$, and **(iv)** C-C•$_6$, where the subscript denotes the number of C–C• defect centres in the conjugated framework. Each atom is plotted as a circle whose area encodes the predicted magnetic-moment magnitude |M|, while color represents the normalized signed error between FT-ChemBERTa and DFT (blue, underestimation; red, overestimation). Insets in each panel enlarge representative regions to highlight clusters of consistent local deviation, predominantly along delocalized ring substructures. The horizontal color bar reports the normalized error range (–1 to +1), and the reference circles to the left of each panel indicate example |M| magnitudes used for visual scaling. Collectively, these maps show that FT-ChemBERTa closely reproduces DFT-level magnetic distributions across extended BioMFM motifs, with residual errors that are spatially interpretable and chemically localized.



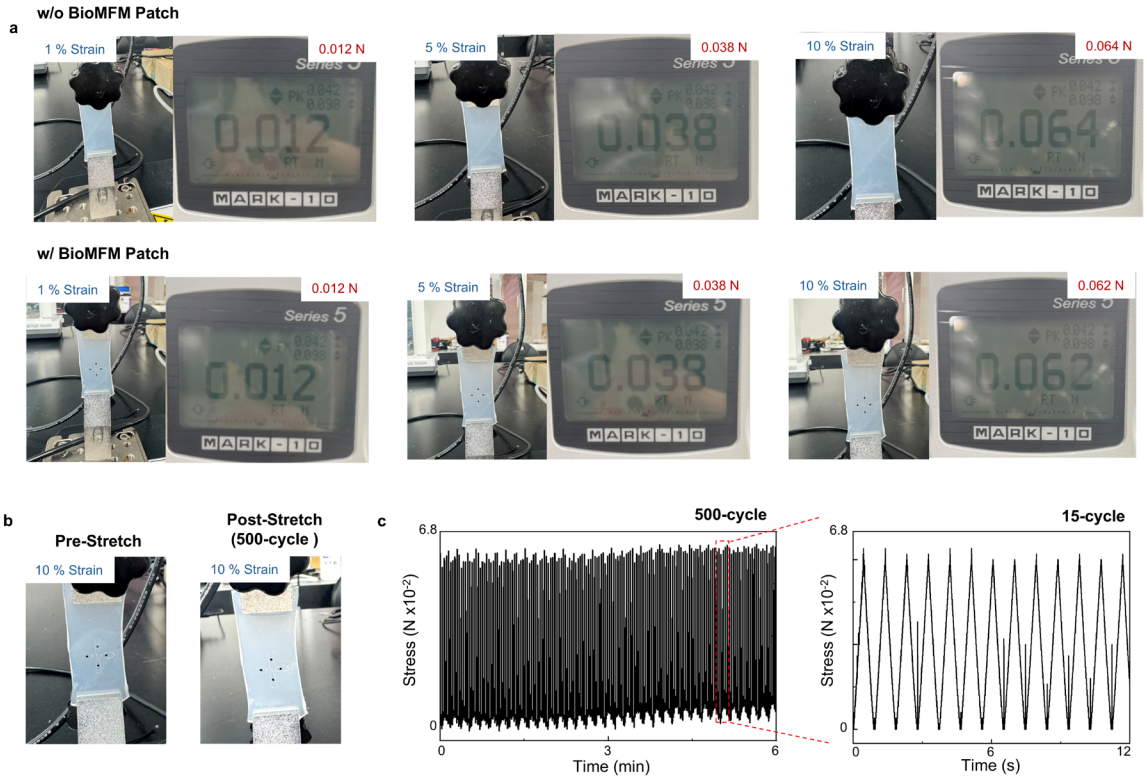
Supplementary Figure 22 Thermo-hygroscopic characterization and actuation of the silk-fibroin robotic layer. a Exploded schematic of the composite module (26 × 6 mm) consisting of a silk-fibroin film, a resistive strain sensor, and a micro-heater encapsulated by PLGA. Differential shrinkage induced by thermally triggered water expulsion drives the controlled bending required for petal blooming (inset: photograph of a bending module at 45 °C; scale bar, 5 mm). **b** Steady-state surface temperature versus input power, demonstrating a near-linear relationship essential for precise set-point control during deployment. **c** Calibration of relative resistance change ($\Delta R/R_0$) versus mechanical strain ($\Delta L/L_0$). **d** Dynamic time traces over repeated heating/cooling cycles, confirming rapid, stable, and reversible actuation. **e** Bending angle as a function of time across a range of 30–50 °C, highlighting tunable actuation amplitudes and accelerated responses at higher temperatures. These results validate the silk-fibroin layer as a reliable temperature-triggered robotic layer capable of achieving self-actuated wet adhesion on the dynamic epicardium.



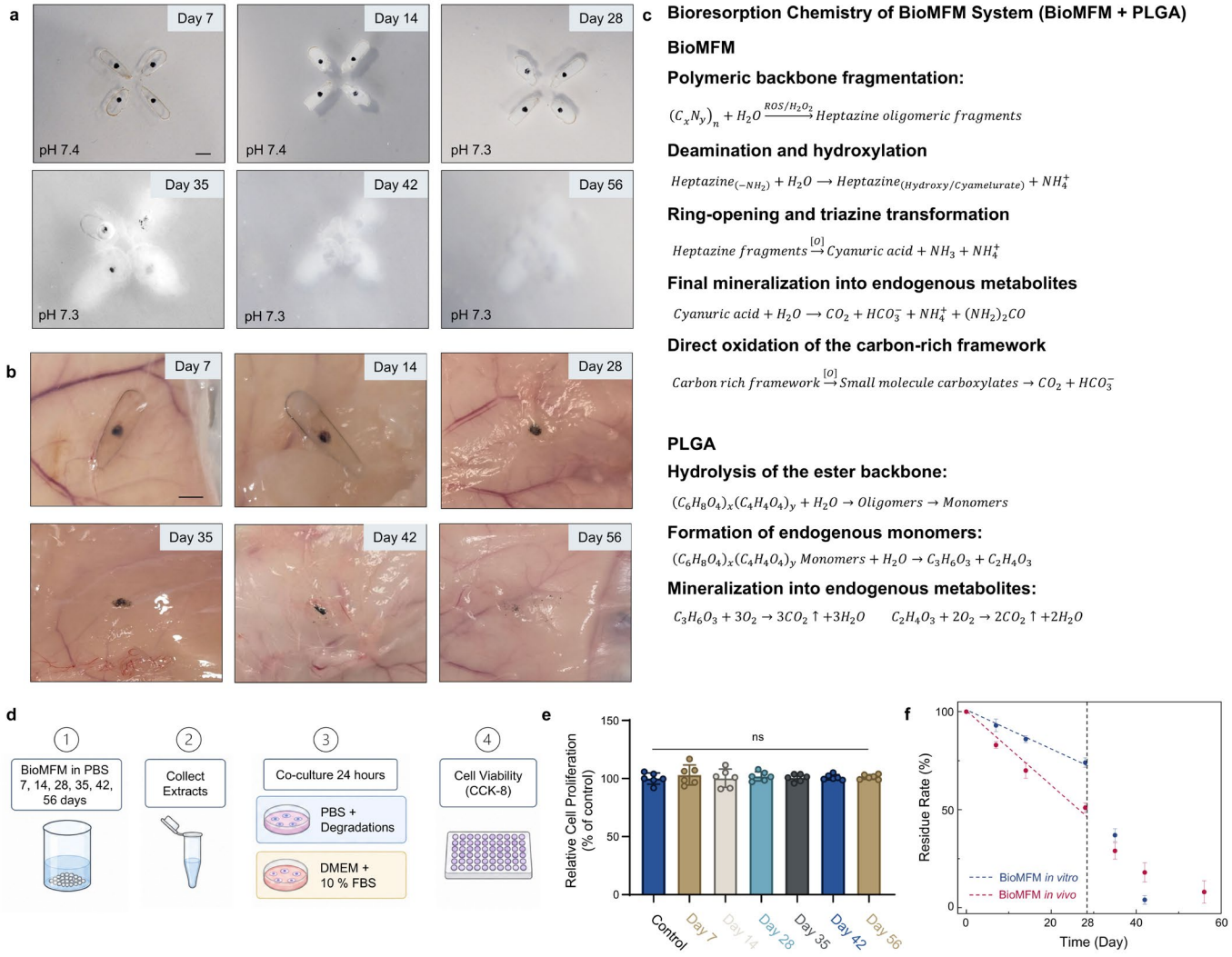
Supplementary Figure 23 Computational modeling of mechanical reliability and deployment kinematics of the BioMFM patch. a Illustration of catheter-guided delivery and bio-triggered "blooming" on the epicardium. The four petals, initially integrated via a transient silk fibroin scaffold, undergo target-activated mechanical decoupling upon rapid hydration-induced liquefaction, enabling high-conformance integration with dynamic organ topographies. **b** Schematic of the cyclic "delivery–release–retrieval" loop mimicking intraoperative clinical repositioning fatigue boundaries. **c** Computed von Mises stress evolution profiles across four continuous deployment loops; the overlapping stress states verify excellent elastic structural reproducibility and framework fatigue durability. **d** Localized stress and strain distributions mapping the mechanics within the critical hinge regions. Owing to the reduced local bending radii, the maximum von Mises stress is concentrated at the folding roots, whereas the strain across the petal surfaces remains comparatively low ($\varepsilon_{VMS} \leq 5.8 \times 10^{-2}$), indicating a substantial mechanical safety margin under the modeled deployment conditions.



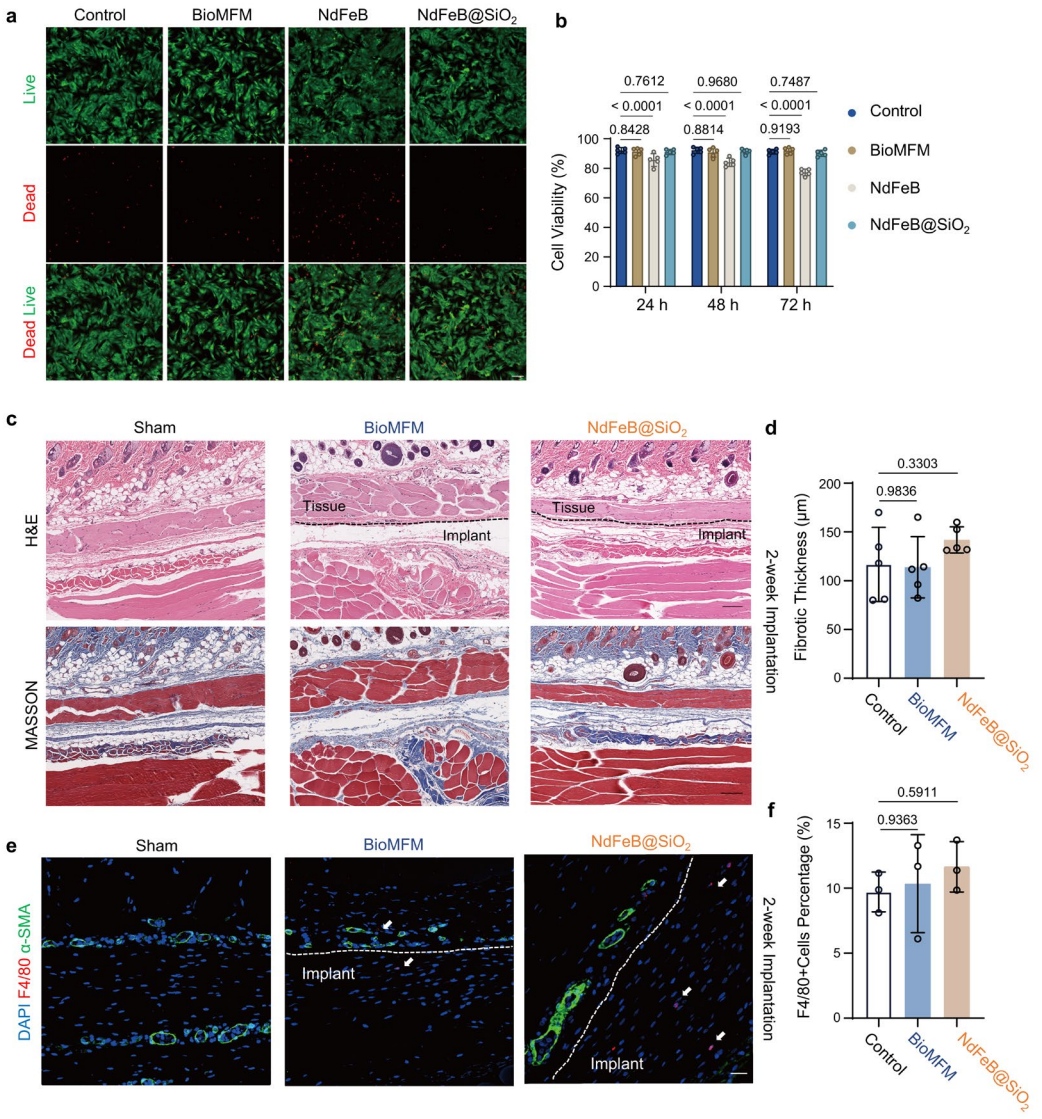
Supplementary Figure 24 Structural memory longevity and cyclic relocation fatigue boundaries of the BioMFM patch. a Time-course verification of shelf-life reliability under ambient desiccated storage over a 35-day horizon (scale bar, 5 mm). The chronological comparison demonstrates invariant kinematic fidelity and shape-memory retention between pristine and 5-week-aged scaffolds. **b** High-strain cyclic fatigue testing inside a mock catheter performed on Day 28 post-fabrication (scale bar, 5 mm). The overlapping configurations across 6 consecutive delivery–release–retrieval loops confirm excellent structural cohesion and elastic reversibility, featuring no visible local mechanical failure or macroscopic delamination.



Supplementary Figure 25 Nanomechanical compliance and high-cycle interfacial durability of the BioMFM patch. a Comparative tensile loading metrics of bare and patch-stabilized Ecoflex substrates monitored across physiological strain boundaries (1%, 5%, and 10%). **b** Time-course verification of interfacial cohesion during a high-cycle fatigue evaluation involving 500 stretch–relaxation loops at 10% strain. **c** Overlapping stress–strain trajectories (left) and time-resolved cyclic force responses (right) over 15 representative loops, verifying that the patch imposes minimal additional mechanical loading on the underlying elastomeric matrix.

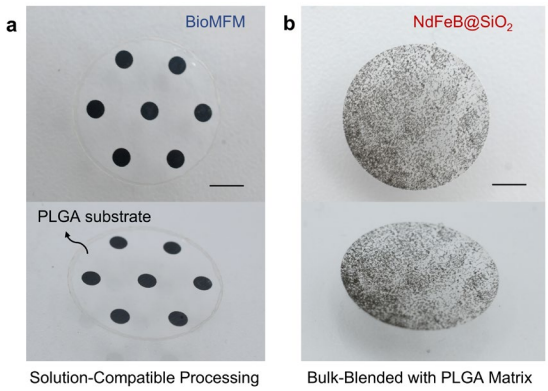


Supplementary Figure 26 Degradation pathways, cytocompatibility profiles, and multi-environment clearance kinetics of the BioMFM scaffold. a Chronological optical tracking of the structural dissociation and morphological breakdown of the trilayer patch in PBS (pH 7.4, 37 °C) up to Day 56. The annotated pH values demonstrate remarkable microenvironmental stability (from 7.4 to 7.3) throughout the 8-week period (scale bar, 2 mm). **b** Longitudinal in vivo gross-morphological images monitoring the implant site from Day 7 to Day 56, illustrating progressive tissue-mediated resorption and benign encapsulation in situ (scale bar, 2 mm). **c** Potential chemical mechanism showing the oxidation-assisted hydrolysis pathways of the co-degrading BioMFM/PLGA matrix. **d** Methodological workflow for temporal intermediate harvesting across six degradation milestones and subsequent 24 h co-culture tracking. **e** Cellular metabolic viability assessed using CCK-8 assays following exposure to time-course degradation extracts. No statistically significant differences were observed (ns, not significant). **f** Comparative residual-mass profiles during parallel in vitro aqueous degradation and in vivo subcutaneous resorption over 56 days. For **e** and **f**, data are mean ± s.d.; n = 6 biologically independent samples per group for **e**; n = 3 independently prepared BioMFM patches for the in vitro measurements and n = 3 biologically independent animals for the in vivo measurements at each time point for **f**. Statistical significance in **e** was assessed using ordinary one-way ANOVA followed by Dunnett's multiple-comparisons test (two-sided), with adjustment for multiple comparisons.

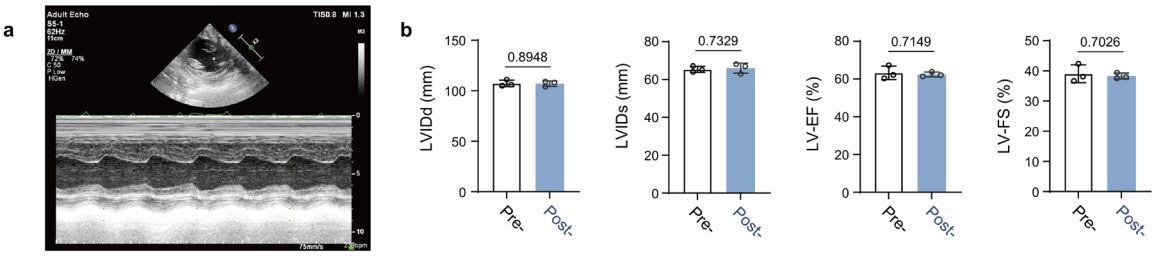


Supplementary Figure 27 Comprehensive in vitro cytocompatibility and early-stage in vivo histocompatibility of magnetic biomaterials. a Representative fluorescence micrographs of cells co-cultured with material extracts, stained with a live/dead assay (green: live cells; red: dead cells) (scale bar, 100 μm). **b** Quantitative cell viability tracking over 24 h, 48 h, and 72 h relative to the untreated negative Control. While bare NdFeB induces severe, acute cytotoxicity ($P < 0.0001$), both BioMFM and NdFeB@SiO_2 maintain high, non-toxic cell viability comparable to the control group across all chronological checkpoints. **c** Cross-sectional hematoxylin and eosin (H&E) and Masson's trichrome staining images of peri-implant subcutaneous tissues collected at the early 2-week post-implantation milestone (Sham group serves as control). Dashed lines demarcate the implant–tissue interfaces (scale bar, 100 μm). **d** Quantitative statistical benchmarking of localized fibrotic capsule thickness at 2 weeks post-implantation, confirming no statistically significant deviations among the cohorts ($P > 0.3$). **e** Representative confocal immunofluorescence micrographs of peri-implant tissues at the 2-week milestone stained for nuclei (DAPI, blue), macrophages (F4/80, red), and myofibroblasts/vessels (α-SMA, green). Dashed lines indicate tissue–implant borders; white arrows highlight localized $F4/80^+$ inflammatory cells (scale bar, 20 μm). **f** Quantitative analysis of localized $F4/80^+$ macrophage infiltration densities within the subcutaneous matrix. Consistent with the intact temporary shielding afforded by the

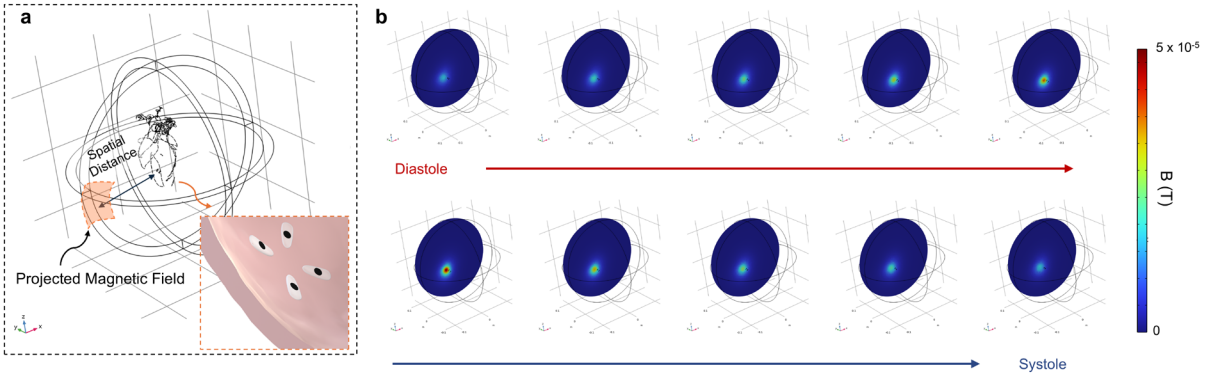
silica shell during this acute phase, both the BioMFM and NdFeB@SiO_2 cohorts maintain uniform, low-level inflammatory infiltration that remains statistically indistinguishable from the healthy Sham controls ($P > 0.5$). For **b**, **d**, and **f**, data are mean ± s.d.; n = 5 biologically independent samples per group for **b**; n = 5 biologically independent animals per group for **d**; n = 3 biologically independent animals per group for **f**. Similar histological findings shown in **c** were observed in five biologically independent animals per group. Similar staining patterns shown in **e** were observed in three biologically independent animals per group. Statistical significance in **b** was assessed using two-way ANOVA; ordinary one-way ANOVA was used in **d** and **f**. Dunnett's multiple-comparisons test (two-sided) was applied for post hoc comparisons, with adjustment for multiple comparisons.



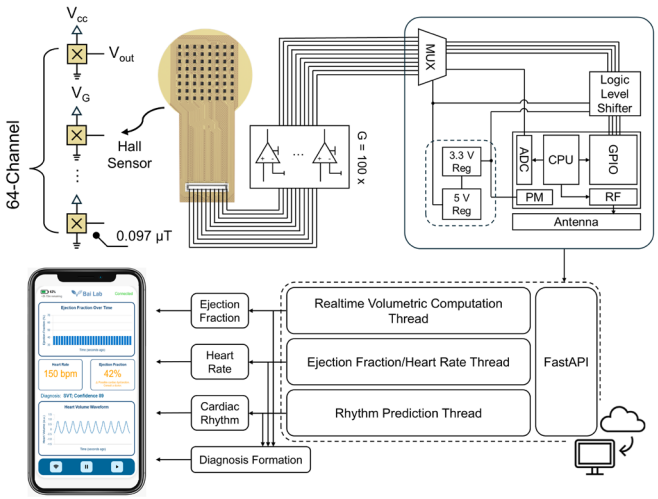
Supplementary Figure 28 Structural configurations and fabrication paradigms of BioMFM and inorganic composite patches. a Top and perspective views of the solution-processed BioMFM thin-film patch (scale bar, 5 mm). Powdered BioMFM (~20 mg) was uniformly dispersed and directly drop-cast as a continuous, compliant layer onto a flexible PLGA substrate. **b** Top and perspective views of the metallic inorganic control patch (scale bar, 5 mm). Granular NdFeB@SiO_2 particles (~20 mg) were bulk-blended into a viscous PLGA matrix to form a heterogeneous particulate composite architecture.



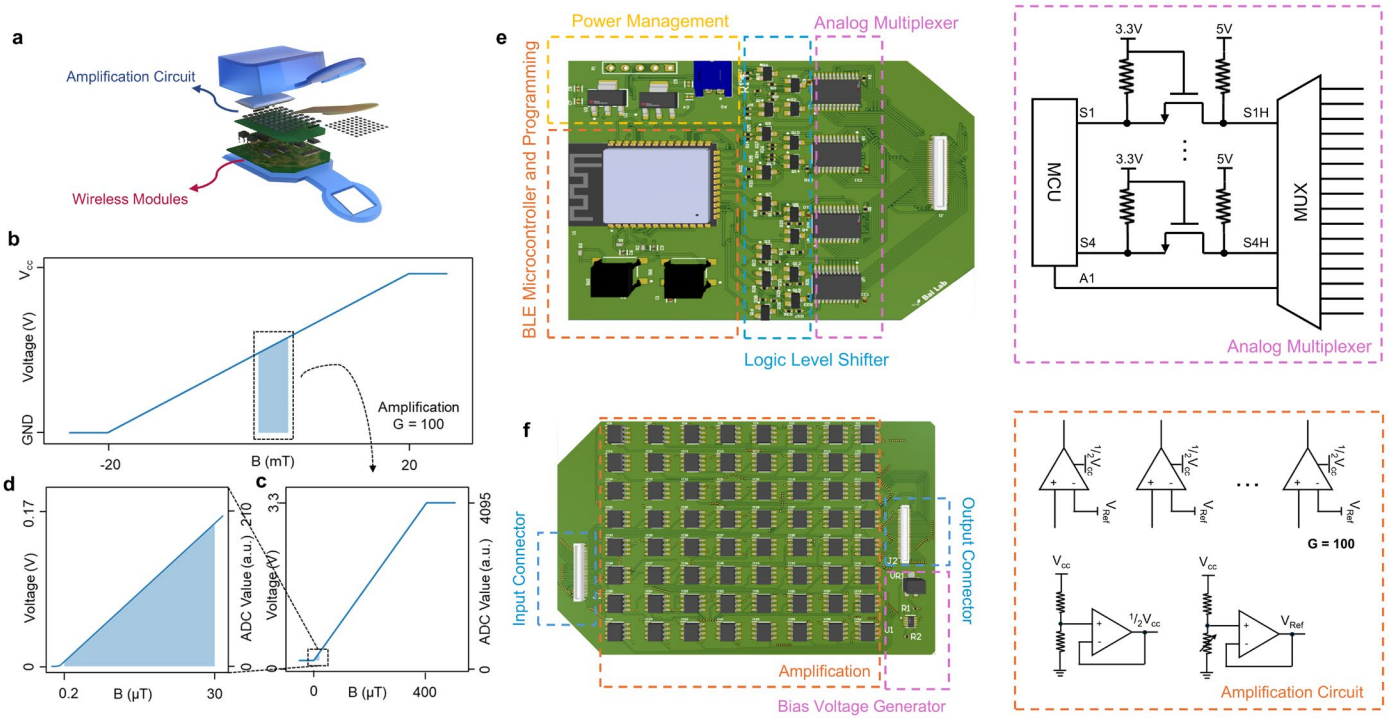
Supplementary Figure 29 In vivo echocardiographic evaluation and mechanical safety profiling of baseline cardiac function. a Representative M-mode echocardiograms recorded before and after epicardial patch deployment. **b** Quantitative statistical benchmarking of left ventricular internal diameter at diastole (LVIDd), left ventricular internal diameter at systole (LVIDs), left ventricular ejection fraction (LV-EF), and left ventricular fractional shortening (LV-FS) measured immediately before (white bars) and after (blue bars) BioMFM patch attachment. Individual data points represent independent biological replicates. Statistical significance was determined by a paired two-tailed Student's t-test; exact P values are indicated directly above the bars, confirming that the mechanical presence of the conformable patch introduces zero functional or restrictive impairment to native left ventricular contractility.



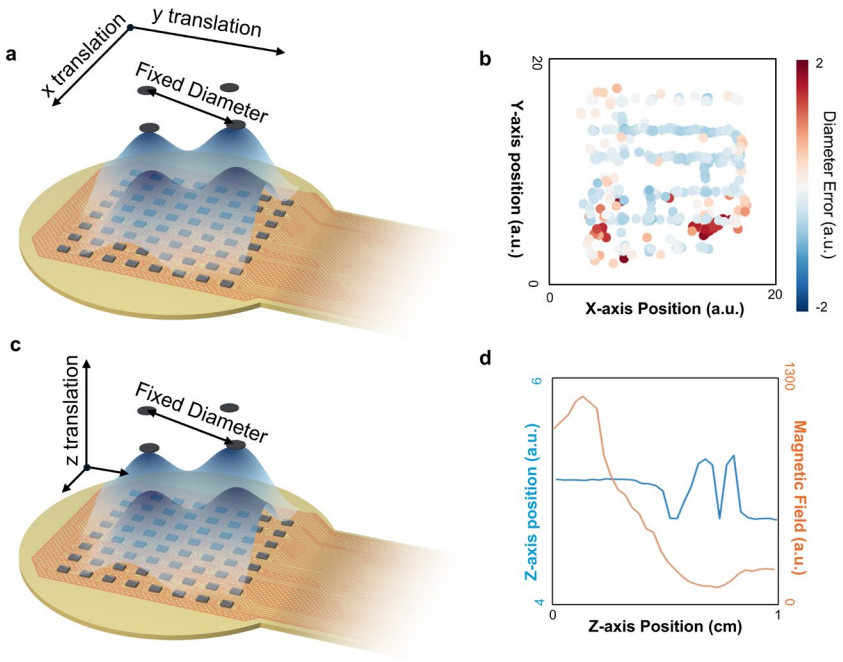
Supplementary Figure 30 Computational modeling of magneto-mechanical transduction across the cardiac cycle. a Schematic of four bloomable BioMFM implants positioned on the left ventricular epicardium, serving as high-fidelity magnetic tracers for intrinsic myocardial mechanics. As the heart translates and deforms during the cardiac cycle, the spatial distance and orientation of the implants evolve relative to the external sensing plane, generating distinct projected magnetic-field variations. **b** FEA results of the magnetic flux density magnitude on the sensing plane over one representative cardiac cycle (color bar, |B|). The upper row resolves the transition from early-to-late ventricular diastole, and the lower row captures the progression of ventricular systole. These simulations verify that myocardial dynamics are effectively transduced into deep-tissue magnetic signatures, facilitating continuous, untethered monitoring robust against tissue impedance.



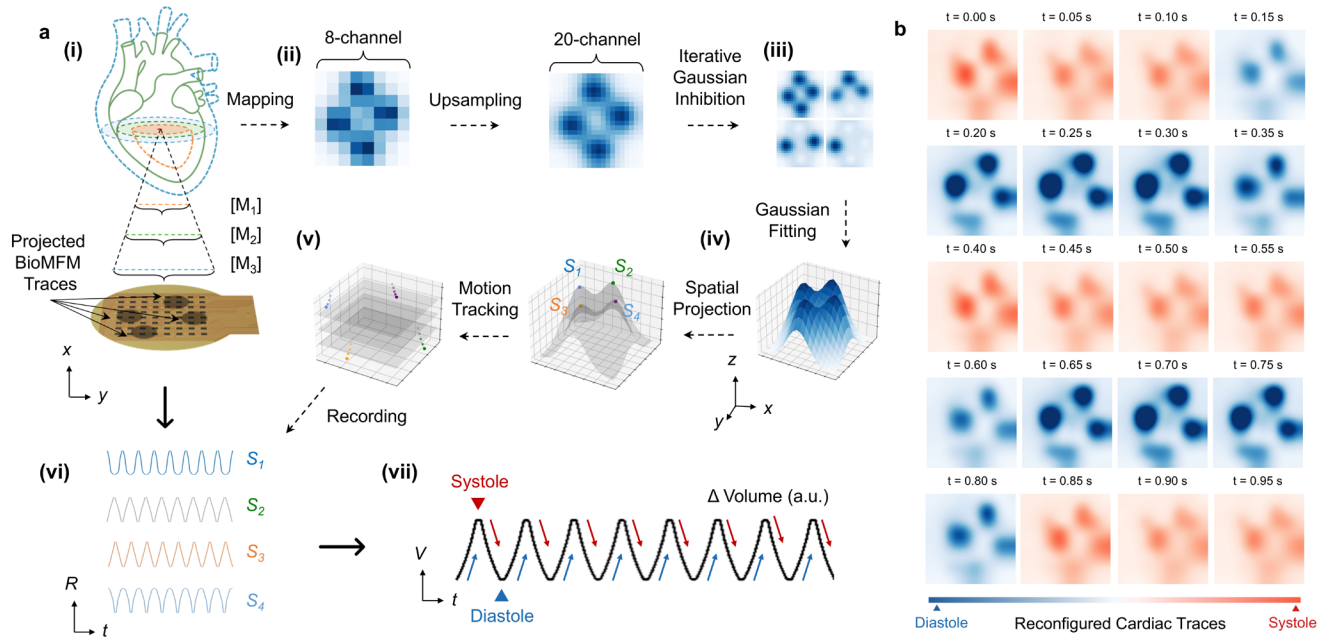
Supplementary Figure 31 System-level architecture and cloud-integrated pipeline of the wearable BioMFM reader. A 8 × 8 (64-channel) Hall-effect sensor array converted local magnetic flux density from implanted BioMFM sources into voltages with a nominal sensitivity of ~0.097 μT, which were amplified (gain ≈ 100) and routed through an analog multiplexer to a low-power microcontroller unit (MCU). The MCU sequentially digitized the amplified signals, packaged the time-domain data streams, and transmitted them wirelessly via Wi-Fi to a smartphone-linked gateway and cloud server. On the server side, parallel software threads performed real-time volumetric reconstruction of left-ventricular motion, ejection-fraction and heart-rate estimation, and rhythm classification, with processed results returned to a mobile dashboard for user visualization and clinical interpretation.



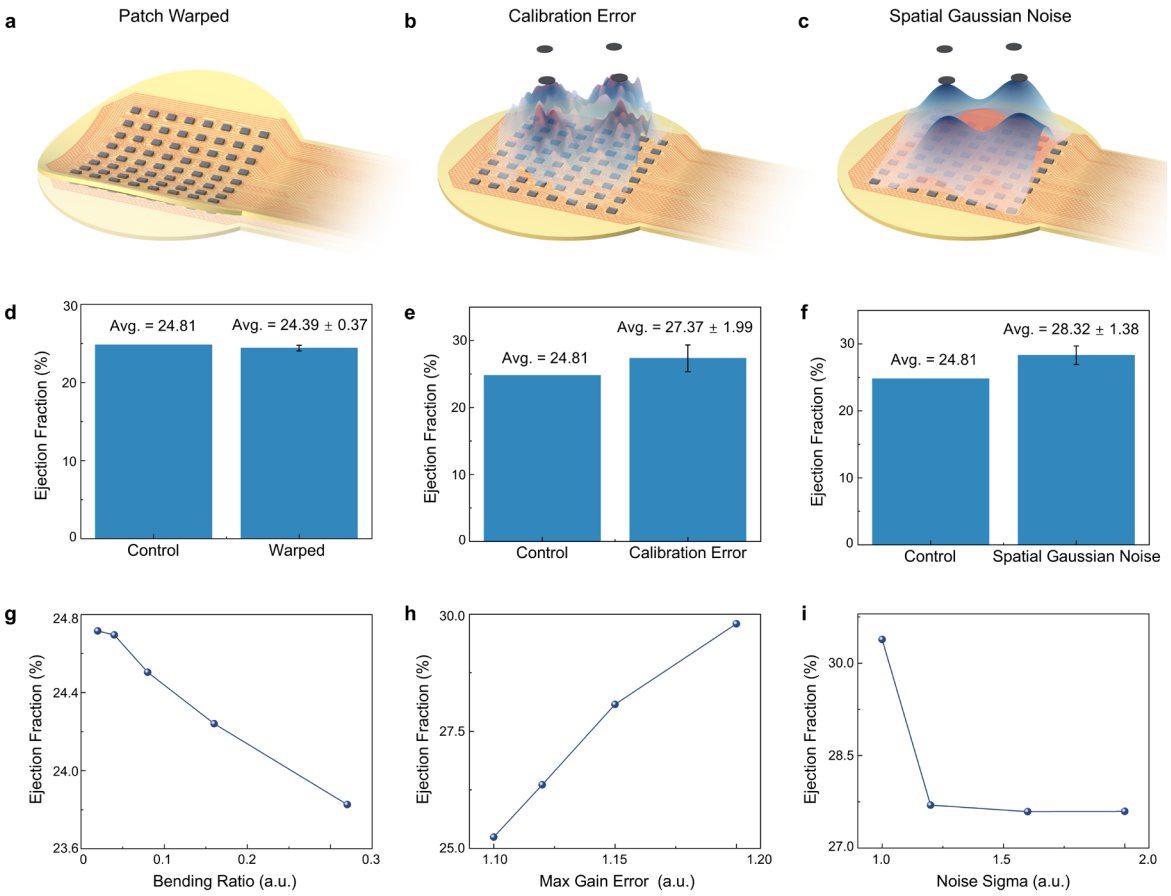
Supplementary Figure 32 Hardware architecture and signal characterization of the wearable Hall-effect sensing system. a Exploded diagram of the hall-effect sensor array as well as amplification and wireless modules. **b–d** Electrical transfer characteristics of a representative Hall sensor. **b** Unamplified output voltage versus magnetic flux density, exhibiting a linear response from −20 to +20 mT with saturation outside this range. **c** Response after fixed-gain amplification (G = 100), expanding the useful range to ~0–400 μT. **d** Magnified view of the amplified response in the BioMFM operating window (≈ 0.2–30 μT); the voltage change was digitized by a 14-bit ADC, yielding ~2^{12} resolvable steps and an effective field sensitivity of ~0.097 μT per least significant bit. **e** Rendered circuit board and schematic of the wireless module. An ESP32-S3 microcontroller controls the analog multiplexers via N-MOSFET-based logic-level shifters to sequentially sample all 64 amplified Hall outputs before digitization and wireless transmission. **f** Rendered circuit board and schematic of the amplification module. Sixty-four precision, fixed-gain (G = 100) differential amplifiers interface with the Hall array; an on-board buffered potentiometer sets an adjustable common-mode bias, and a buffered voltage divider provides the reference voltage for differential amplification.



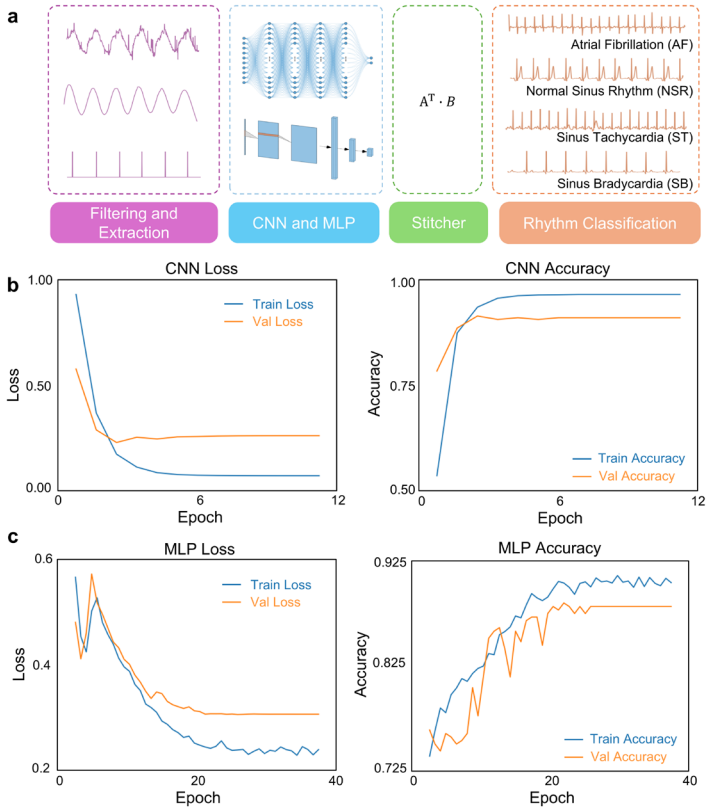
Supplementary Figure 33 Computational validation of the PAGO-DeMag algorithm for motion-robust cardiac reconstruction. a Schematic of four-petal BioMFM implants forming an approximate circumcircle above the 8 × 8 Hall-sensor array, with a smooth magnetic-field surface reconstructed from simulated sensor readings; only the centroid of the circumcircle is translated in the x–y plane to mimic chest-wall sliding. **b** Map of the relative error in the reconstructed circumcircle radius across different centroid positions on the array, showing uniformly low error despite large in-plane translation. **c** Schematic of the same four-petal configuration undergoing rigid displacement along the z-axis (normal to the array), while the projected circumcircle radius is preserved. **d** PAGO-DeMag reconstruction of z-axis position (blue, left axis) and corresponding magnetic-field amplitude at the array (orange, right axis) as the source–sensor distance is increased, demonstrating accurate recovery of the circumcircle radius even as the measured field strength decays. Together, these simulations show that PAGO-DeMag separates global translation from intrinsic concentric/eccentric motion, enabling robust estimation of volumetric cardiac dynamics from surface magnetic-field measurements.



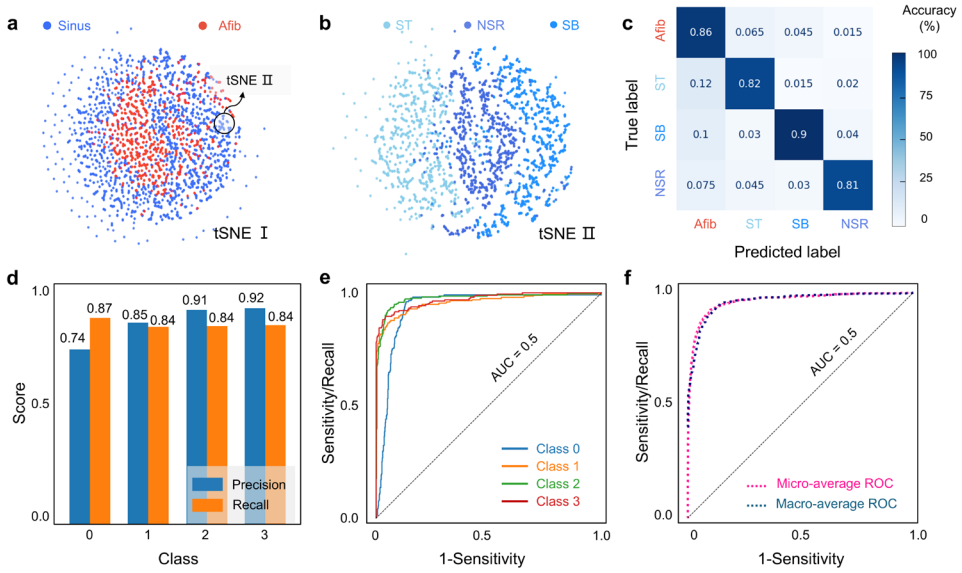
Supplementary Figure 34 Workflow and dynamic implementation of the PAGO-DeMag algorithm for cardiac volumetry. a Schematic of four-petal BioMFM implants on the left ventricle and **(i)** their projected magnetic field on an external 8 × 8 Hall-sensor array during a cardiac cycle. **(ii)** Example low-resolution (8 × 8) magnetic-field frame acquired by the array and its interpolation to a dense 20 × 20 map. **(iii)** Iterative Gaussian-inhibition step, in which the global maximum on the interpolated map is detected and its neighborhood is multiplicatively suppressed with a Gaussian kernel; the detect–inhibit loop is repeated until no remaining peaks exceed a set threshold, yielding initial peak locations. **(iv)** Physics-constrained multi-Gaussian fitting step that refines predicted source positions and amplitudes (S_1–S_4) so that the summed Gaussian surfaces reproduce the measured field. **(v)** The predicted peak locations were tracked over time to produce tracings of the four individual source trajectories over time. **(vi)** A least-squares circumcircle is fitted to the four predicted peak locations. **(vii)** The cubed circumcircle radius (R^3) is used as a surrogate for chamber volume (ΔV). **b** Sequence of 20 consecutive interpolated frames (interval = 0.05 s) over two representative cardiac cycles, as moving from systole (red-enhanced high field) toward diastole (blue-dominant low field) and back.



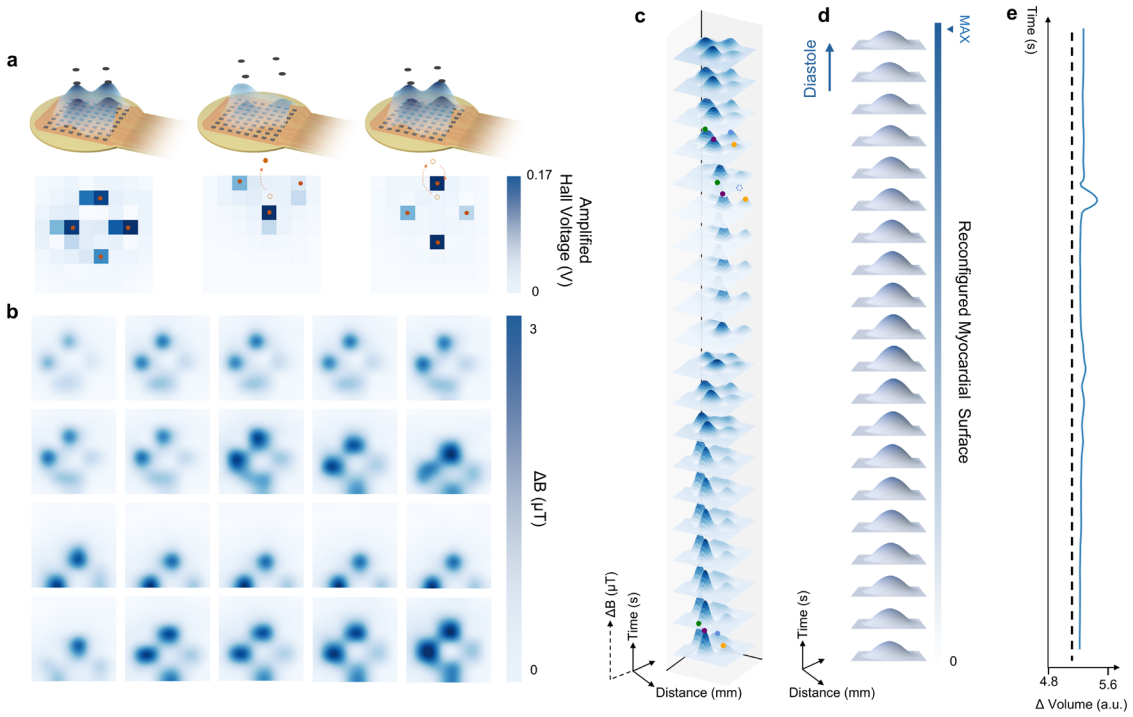
Supplementary Figure 35 Quantitative sensitivity analysis of the PAGO-DeMag algorithm against geometric, calibration, and noise-induced sensor non-idealities. a-c Structural schematics visualizing the three simulated error-inducing hardware regimes superimposed on the flexible skin-conformal Hall array matrix, encompassing **a** geometric patch warping/bending, **b** random channel-wise calibration gain errors, and **c** additive spatial Gaussian noise. **d-f** Statistical comparisons benchmarking the baseline expected cardiac ejection fraction (Control = 24.81%) against the algorithmic predictions decoded from corrupted sensor datasets **d** under patch warping (24.39% ± 0.37%), **e** severe calibration gain drift (27.37% ± 1.99%), and **f** high-amplitude spatial noise (28.32% ± 1.38%). **g-i** Graded tracking trajectories mapping the parametric sensitivity of the decoded ejection fraction as **g** a continuous function of the bending ratio, **h** maximum gain error boundaries, and **i** spatial noise sigma levels. For **d-f**, data are presented as mean ± s.d. calculated across the simulated parameter settings shown in **g-i**, respectively (n = 5 parameter settings for **d**; n = 4 for **e**; n = 4 for **f**). The Control value represents the unperturbed reference simulation.



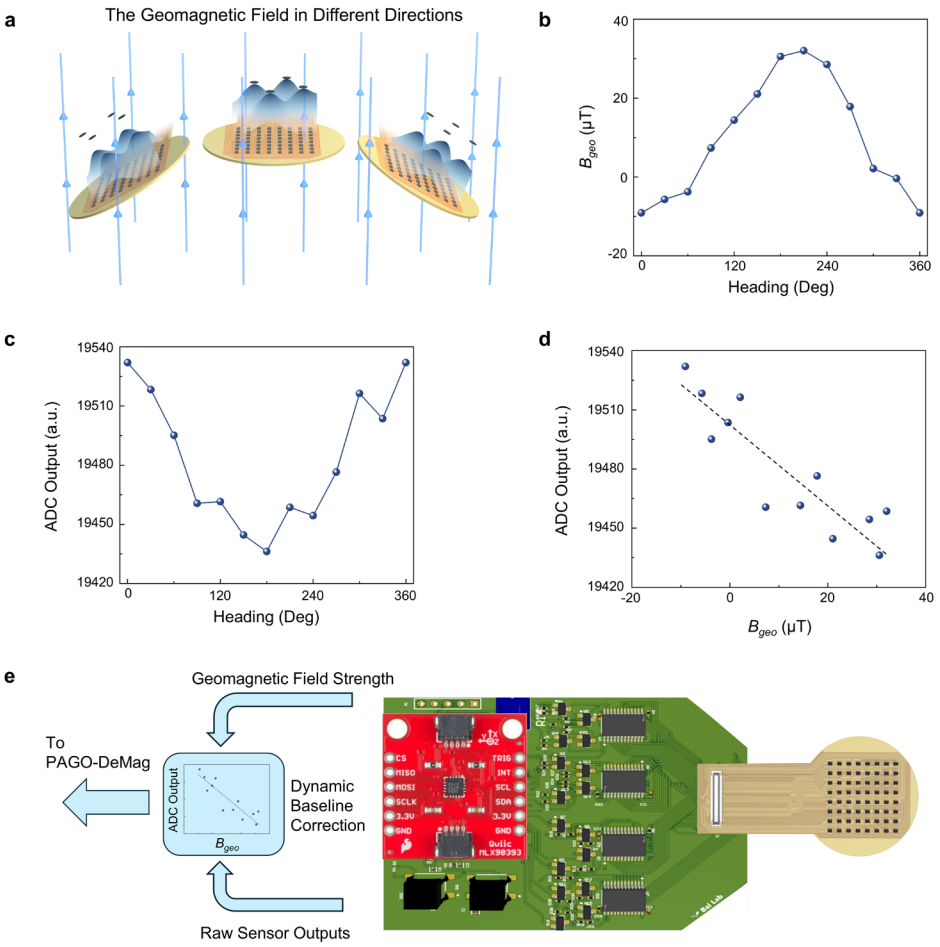
Supplementary Figure 36 Machine-learning pipeline for rhythm classification from BioMFM-derived volumetric traces. a Schematic workflow of the rhythm-classification model: continuous volumetric traces obtained from PAGO-DeMag were low-pass filtered, peak locations were identified, and two feature streams were formed. Specifically, a peak-annotated time series was fed into a 1D convolutional neural network (CNN), whereas beat-to-beat (RR-interval) features were fed into a multilayer perceptron (MLP). Outputs from the CNN and MLP branches were combined by an untrained "stitcher" layer to yield final predictions of cardiac rhythm. **b** Training and validation loss and accuracy curves for the CNN branch, showing progressive loss reduction and rising accuracy with limited overfitting. **c** Corresponding training histories for the MLP branch, likewise demonstrating rapid convergence and stable validation performance. Together, these results indicate that BioMFM-based volumetric recordings contain sufficient information for reliable, real-time rhythm classification.



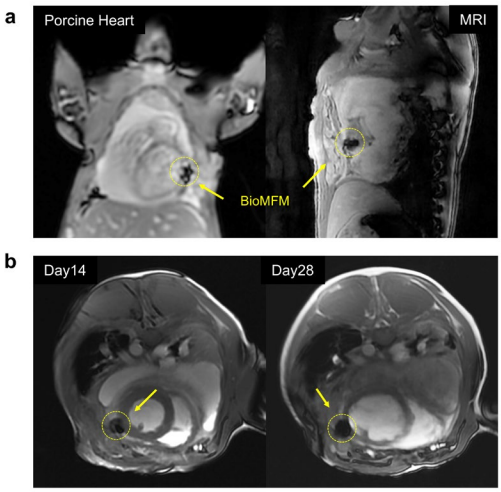
Supplementary Figure 37 Rhythm classification performance from BioMFM-derived volumetric traces. a t-distributed stochastic neighbor embedding (t-SNE) visualization of latent features learned by the CNN–MLP model for binary classification of sinus rhythm versus atrial fibrillation (Afib), showing separable clusters in the embedded space. **b** t-SNE visualization for the four-class states: sinus tachycardia (ST), sinus bradycardia (SB), normal sinus rhythm (NSR), and Afib, demonstrating distinct manifolds for each rhythm. **c** Normalized confusion matrix summarizing model predictions across the four rhythm classes, with strong values along the diagonal indicating high correct-classification rates. **d** Bar plots of per-class precision and recall, with numeric values labeled above each bar, showing uniformly high performance across rhythms. **e** One-versus-rest receiver-operating characteristic (ROC) curves for each class, illustrating high area under the curve (AUC) values relative to the chance line (AUC = 0.5). **f** Micro- and macro-averaged ROC curves, further confirming robust overall discriminative performance. Together, these analyses demonstrate that BioMFM-based volumetric sensing, coupled with lightweight deep-learning models, accurately distinguishes multiple cardiac rhythm states.



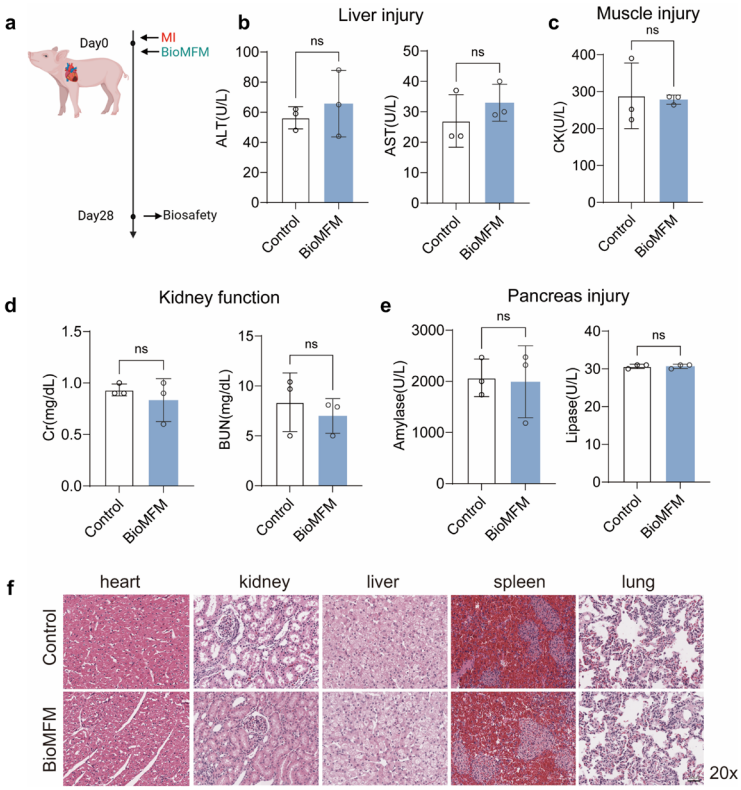
Supplementary Figure 38 Algorithmic robustness and signal integrity of PAGO-DeMag under partial magnetic source dropout. a Schematic of four BioMFM implants on the ventricular wall as the heart slides relative to the external 8 × 8 Hall-sensor array, causing one implant to move progressively beyond the array footprint and fall out of the sensing field. **b** Measured low-resolution magnetic-flux maps from the Hall array at successive time points during this dropout experiment, showing the disappearance of one of the four peaks as its source moves out of range. **c** Gaussian-fitted magnetic field distributions of the experimental recordings over time. **d** Reconstructed circumcircle and inferred volumetric contour derived from the remaining sources over time, illustrating that both chamber radius and centroid position are stably estimated despite loss of one magnet. **e** Normalized volumetric trace obtained from the circumcircle radius compared with the ideal reference (dashed line), demonstrating preserved systolic–diastolic modulation and minimal distortion. Together, these data show that the PAGO-DeMag–enabled BioMFM system tolerates motion-induced partial source dropout and maintains reliable estimation of cardiac volume dynamics, demonstrating robustness to motion artifacts.



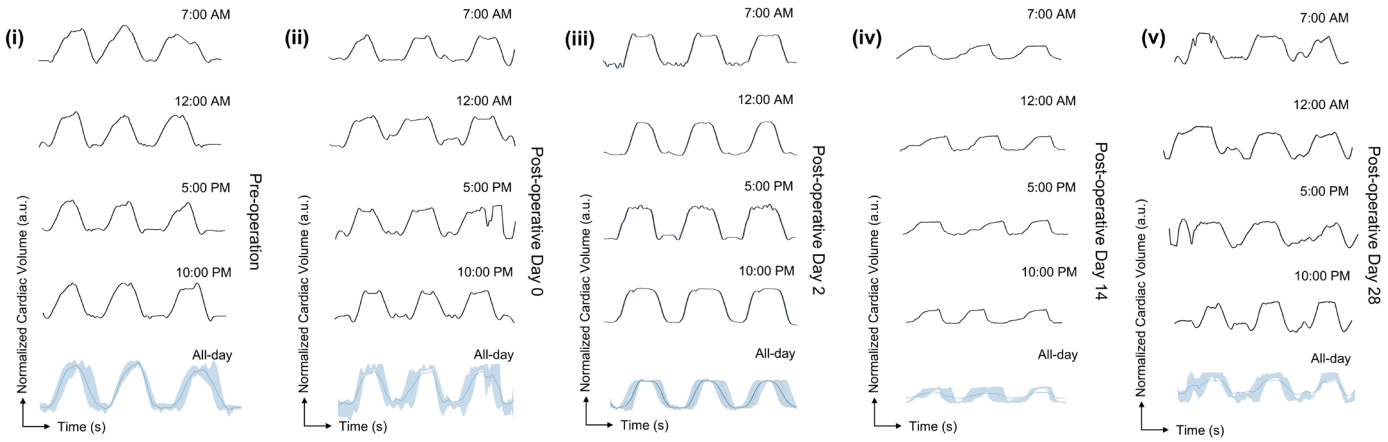
Supplementary Figure 39 Co-planar hardware loop and dynamic common-mode vector field cancellation for ambulatory geomagnetic noise suppression. a Schematic diagram illustrating the parallel, spatially uniform layout of the background geomagnetic field vector slicing through the flexible Hall sensing array under variable angular orientation headings and tilting. **b** Real-time geomagnetic field fluctuations recorded across a full 0°–360° continuous horizontal rotation using our co-planar 3-axis digital reference compass (MLX90393). **c** Synchronized, phase-matched common-mode baseline shifts (ADC Output) captured across identical heading angles by the primary sensing patch matrix. **d** Linear regression transfer function mapping the strict negative correlation established between the reference vector strength and raw array offsets, providing the mathematical matrix for automated real-time subtraction. **e** Complete soft-hardware architecture block layout visualizing the active feedback cancellation loop. The real-time reference vectors are continuously compared with the raw sensor inputs to perform automatic common-mode background subtraction before spatial optimization using PAGO-DeMag.



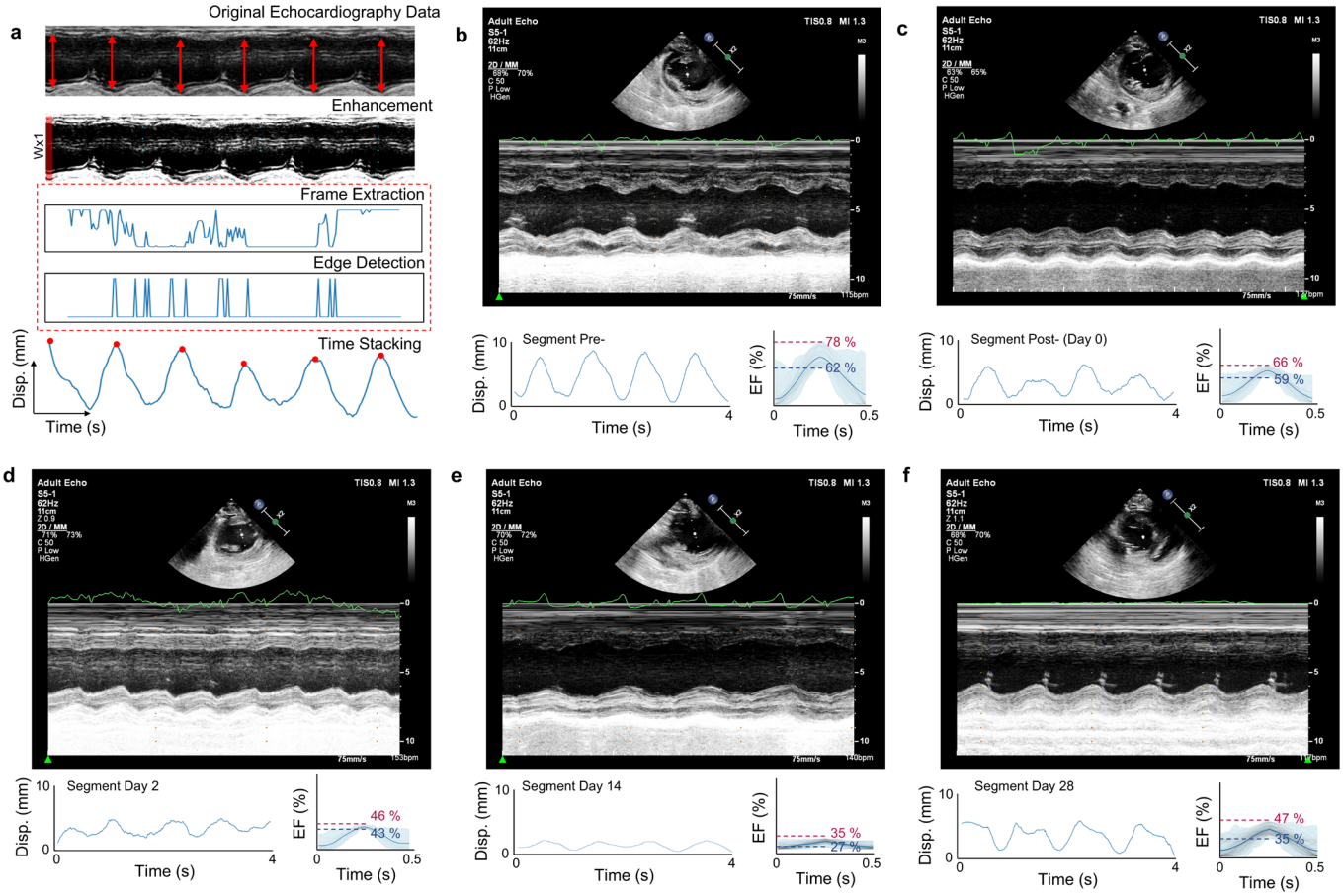
Supplementary Figure 40 In vivo MRI validation of BioMFM epicardial placement and longitudinal stability. a Post-procedural cardiac MRI (3.0 T) acquired in short-axis (left) and long-axis (right) views showing the BioMFM patch positioned on the left-ventricular (LV) epicardial surface (yellow circles/arrows). **b** Serial stability monitoring: Longitudinal short-axis MRI acquired on Day 14 and Day 28 post-implantation. The BioMFM implant maintains persistent visibility and spatial stability at the intended epicardial locus, demonstrating robust adherence to the myocardium despite dynamic cardiac motion and progressive pericardial remodeling over the four-week study period.



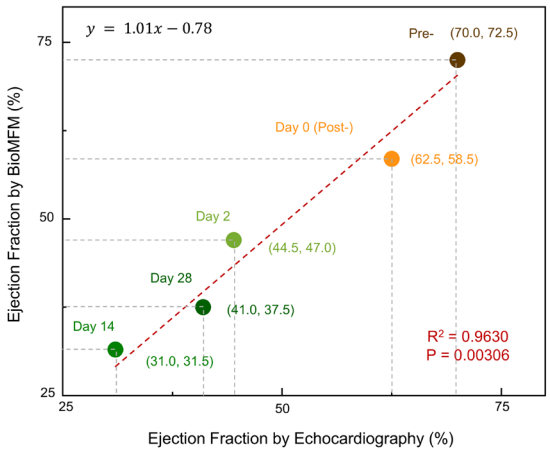
Supplementary Figure 41 Longitudinal systemic biosafety and histopathological evaluation of BioMFM implants. a Experimental workflow: Schematic timeline illustrating the induction of myocardial infarction (MI) and subsequent BioMFM implantation on Day 0, with systemic biosafety assessments performed at the Day 28 endpoint in a porcine model. **b–e** Serum biochemical analysis: Quantitative comparison of metabolic markers between BioMFM-treated animals and MI-only controls. Parameters evaluated include: **b** liver injury (alanine aminotransferase, ALT; aspartate aminotransferase, AST); **c** muscle damage (creatine kinase, CK); **d** renal function (serum creatinine, Cr; blood urea nitrogen, BUN); and **e** pancreatic health (amylase and lipase). No statistically significant differences were observed across any of the clinical indices (ns, not significant). **f** Histology of major organs: Representative hematoxylin and eosin (H&E) sections of the heart, kidney, liver, spleen, and lung harvested at Day 28 (20× objective). Consistent with the biochemical findings, the tissue architecture remains intact with no evidence of localized inflammation, chronic necrosis, or systemic histopathological abnormalities. For **b**–**e**, data are presented as mean ± s.d.; n = 3 biologically independent animals per group. Similar histological findings shown in **f** were observed in three biologically independent animals per group. Porcine model in **a** created in BioRender. Wu, Y. (2026) https://BioRender.com/skvom85.



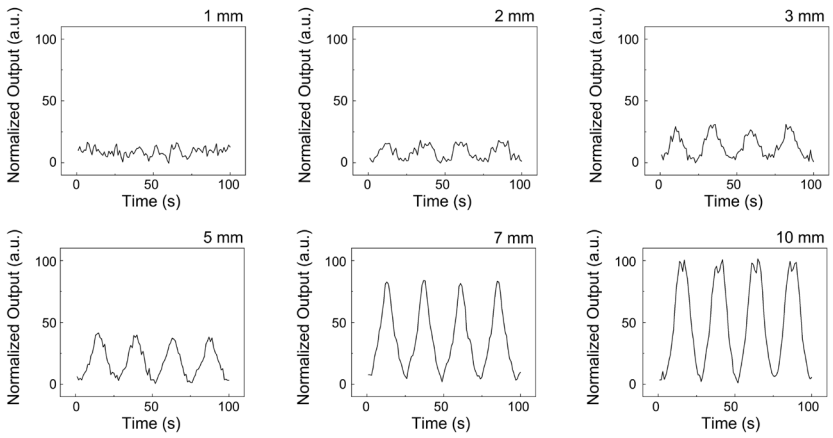
Supplementary Figure 42 Longitudinal all-day cardiac volumetric monitoring across the perioperative window. i-v Representative segments of BioMFM-derived volumetric traces recorded at four distinct time points (7:00 AM, 12:00 PM, 5:00 PM, and 10:00 PM), illustrating the capacity for continuous, stable cardiac functional assessment. The columns track the hemodynamic progression from **(i)** pre-infarction baseline to post-MI stages at **(ii)** Day 0, **(iii)** Day 2, **(iv)** Day 14, and **(v)** Day 28. Within each observation window, the waveforms exhibit exceptional beat-to-beat morphological stability, while the longitudinal series captures the distinct evolution of stroke volume and systolic contractility following the ischemic insult. Bottom row, All-day ensemble averages (solid lines) with variability envelopes (shaded regions), emphasizing the highly reproducible diastolic filling and systolic ejection cycles throughout 24 h of untethered recording. These results confirm the system's high-fidelity performance for long-term physiological monitoring in a dynamic, ambulatory porcine model.



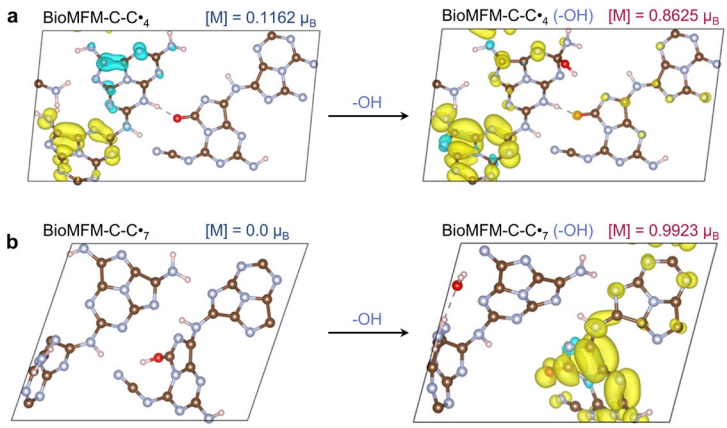
Supplementary Figure 43 Conventional echocardiographic characterization and functional snapshots in the porcine MI model. a Schematic illustrating the extraction of quantitative ventricular trajectories from clinical echocardiograms. M-mode recordings undergo quartile intensity stretching for contrast enhancement, followed by frame-wise slicing and edge detection to generate W × 1 depth-resolved arrays (where W represents the pixel count along the depth axis). Temporal stacking of these features reconstructs the continuous displacement of the ventricular wall. **b-f** Representative parasternal long-axis B-mode images (top), corresponding M-mode recordings through the left-ventricular cavity (middle) and derived ventricular-radius/EF traces (bottom) at selected **b** pre- and **c-f** post-infarction time points. Single EF estimates (percentage values) were obtained from a limited number of beats within each M-mode acquisition, illustrating the operator- and snapshot-dependent nature of echocardiographic assessment in contrast to the continuous volumetric monitoring provided by the BioMFM system.



Supplementary Figure 44 Longitudinal correlation of ejection fraction (EF) measurements between the BioMFM platform and clinical echocardiography. Comparison of EF values derived from the BioMFM sensing system against gold-standard clinical echocardiography. Each data point represents the paired daily mean values obtained at specific milestones across the full pathological trajectory, extracted from **Fig.5g** (BioMFM) and **Supplementary Figure 43** (echocardiography). The red dashed line represents the linear regression fit (y = 1.01x - 0.78), featuring a coefficient of determination (R^2) of 0.9630 and a P value of 0.00306, demonstrating exceptional consistency and high-fidelity tracking of volumetric cardiac dynamics by the BioMFM platform relative to established clinical standards.



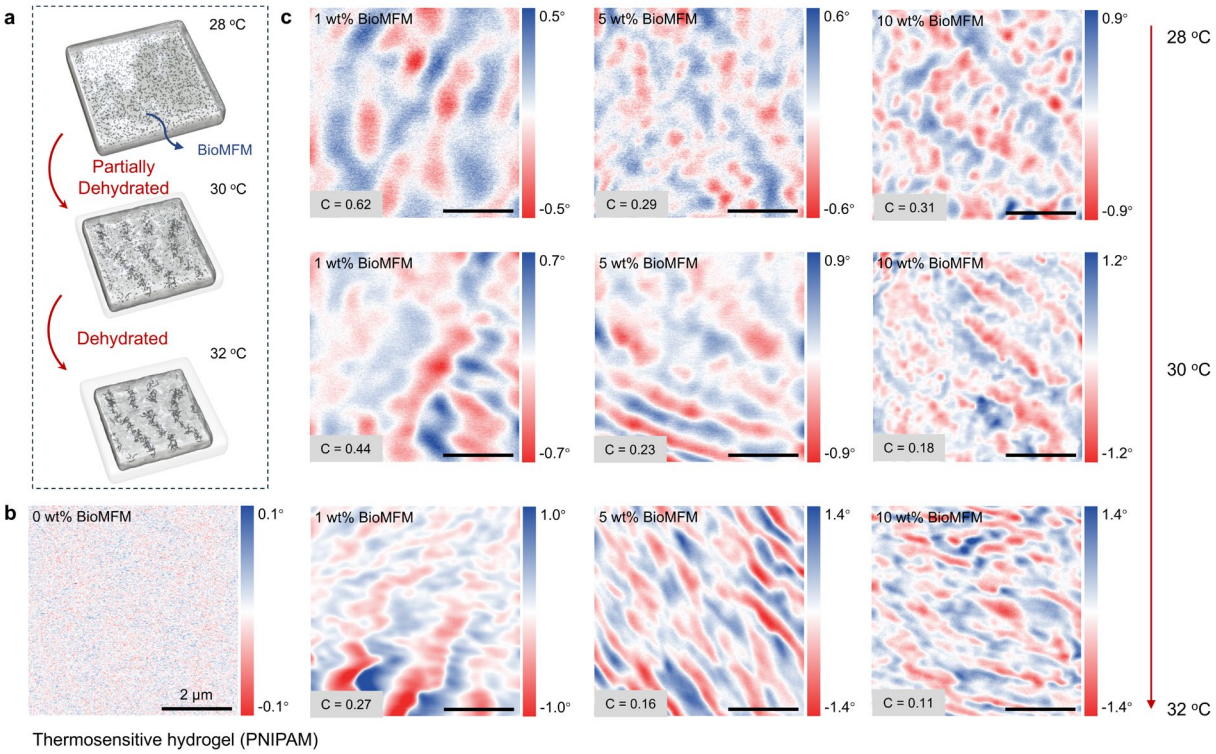
Supplementary Figure 45 Quantitative evaluation of the minimum detectable displacement boundary and cyclic sensitivity profiles. Baseline-corrected temporal trajectories tracking the normalized sensor output as the active BioMFM hydrogel undergoes automated, motorized cyclic displacement cycles at discrete, graded mechanical stroke amplitudes of 1 mm, 2 mm, 3 mm, 5 mm, 7 mm, and 10 mm. The clear, repeatable emergence of a periodic waveform breaking through the baseline fluctuations at 2 mm establishes the minimum detectable displacement under the tested conditions (~2 mm).



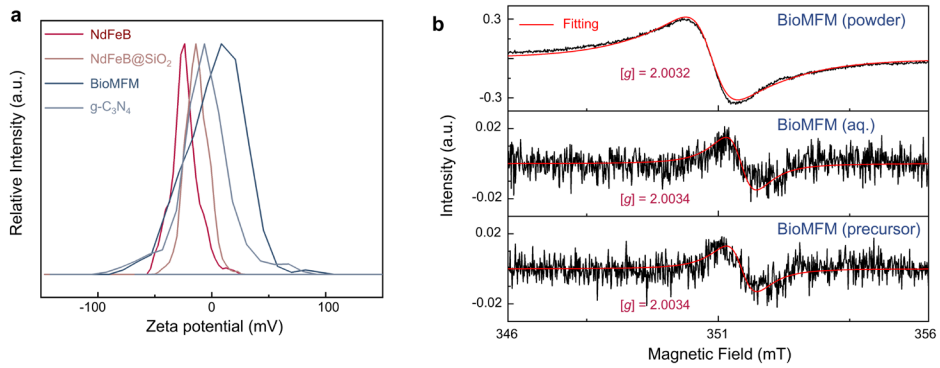
Supplementary Figure 46 Density functional theory modeling of spin-state environmental tolerance. Spatial spin-density isosurface distributions (0.005 e Å^{-3}) mapping representative **a** BioMFM-C-C•$_4$, and **b** BioMFM-C-C•$_7$ configurations before (left) and after (right) localized coordination with polar -OH ligands. The invariant retention and localized amplification of the net magnetic moments verify that the collective exchange splitting and spontaneous magnetization bypass chemical quenching, supporting the persistence of local spin polarization under the modeled polar coordination environment.



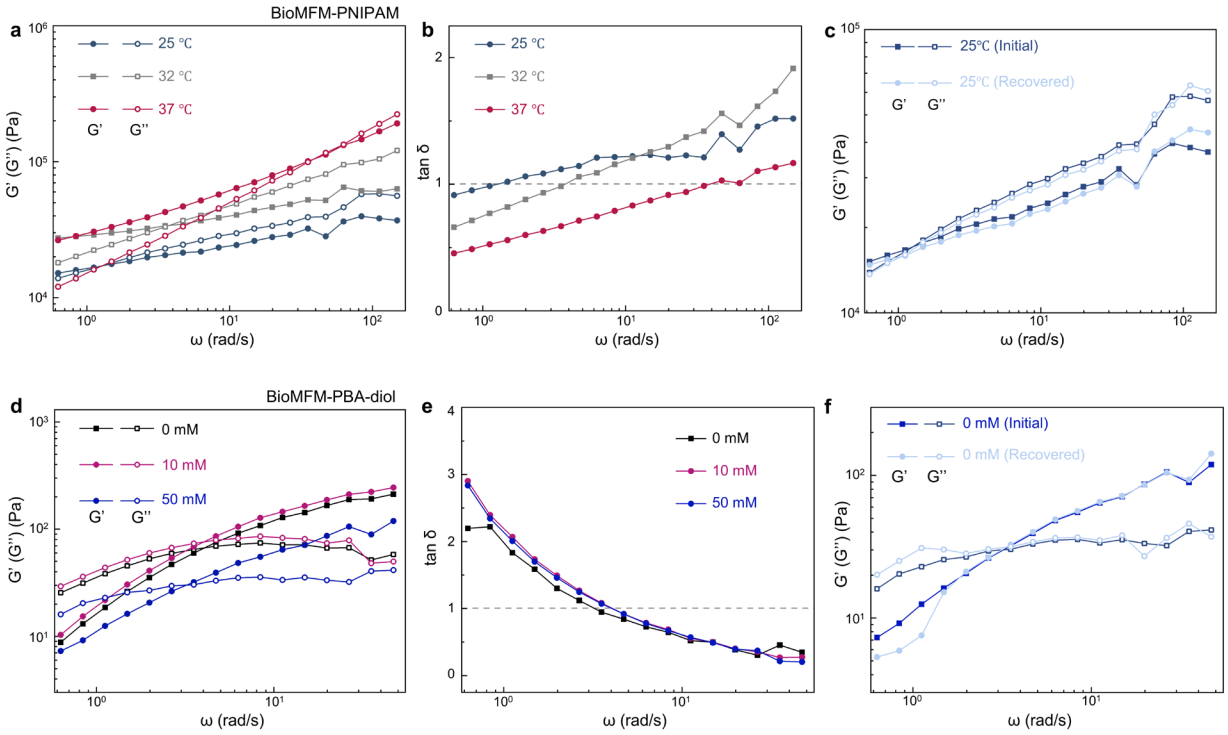
Supplementary Figure 47 Thermoresponsive wettability and hydration-dependent surface characteristics of BioMFM-PNIPAM hydrogels. Sessile-drop water contact angle measurements were performed on thermoresponsive BioMFM-PNIPAM hydrogels to characterize the surface energy transitions that drive in situ mechanical fixation. Images were acquired for compositions containing 1 wt%, 5 wt%, and 10 wt% BioMFM across three distinct hydration/temperature states: **(i)** fully swollen (28 °C); **(ii)** partially dehydrated (30 °C); **(iii)** dehydrated (32 °C). Fully swollen samples exhibited high surface energy with low contact angles (25.3°-26.5°), indicating a highly hydrophilic state. As the temperature increased through the lower critical solution temperature of the PNIPAM matrix, rapid dehydration induced a transition toward increased apparent hydrophobicity, with contact angles rising to 26.4°-39.7° (partially dehydrated) and 43.7°-49.3° (dehydrated). This transition confirms the thermally triggered collapse of the polymer network, facilitating seamless conformability and stable adhesion to warm organ surfaces. At each hydration state, varying the BioMFM loading produced only negligible changes in wettability, demonstrating that the magnetic functionalization does not compromise the matrix's intrinsic thermoresponsive behavior.



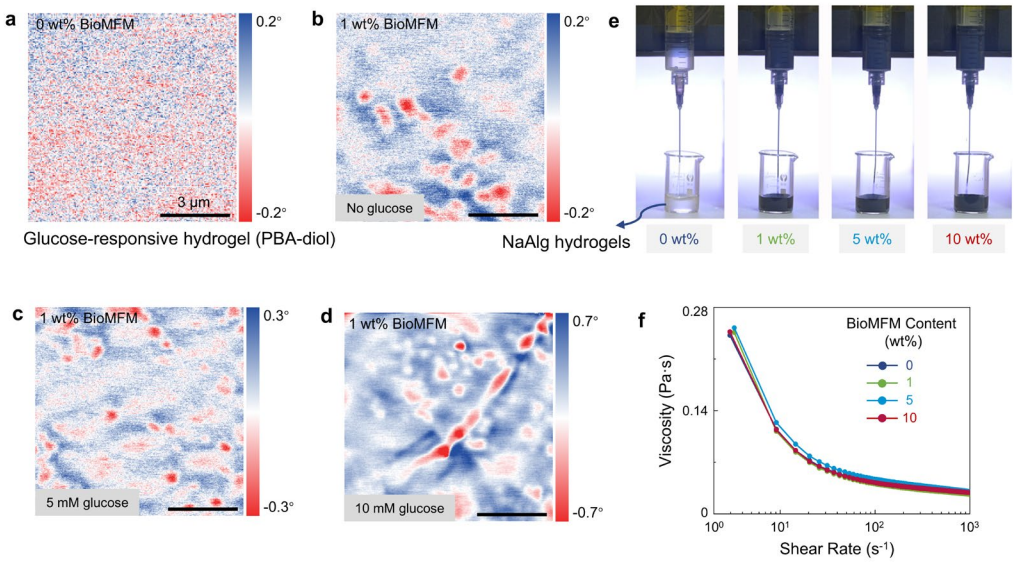
Supplementary Figure 48 Thermoresponsive magnetic domain reconfiguration and structural evolution in BioMFM-PNIPAM hydrogels. a Schematic of the thermoresponsive transition: PNIPAM hydrogels hosting dispersed BioMFM particles undergo localized volume shrinkage upon heating (28 °C-32 °C), driving the spatial redistribution and concentration of embedded magnetic domains to form a robust sensing marker. **b** MFM phase image of a neat PNIPAM hydrogel (no BioMFM) showing negligible phase contrast, indicating the absence of an intrinsic magnetic signal in the polymer matrix (scale bar, 2 μm). **c** MFM phase images of composite hydrogels with varying BioMFM content (1, 5, and 10 wt%) during thermally induced dehydration. With increasing temperature and loading, the magnetic signature evolves from discrete, isotropic spots into elongated, chain-like domains, as quantified by the circularity parameter (C). The decrease in C (*e.g.,* from 0.62 to 0.11 at 10 wt%) reflects redistribution and local concentration of the magnetic stray-field pattern.



Supplementary Figure 49 Electrokinetic profiles and ambient EPR spin-state simulations. a Normalized Zeta-potential distribution spectra tracking liquid-phase sonicated suspensions of bare NdFeB, NdFeB@SiO_2, g-C_3N_4, and BioMFM. While BioMFM exhibits a relatively narrow, positive zeta-potential distribution centred at ~+24.4 mV, metallic configurations (NdFeB, NdFeB@SiO_2) feature broad, bipolar distributions, inducing macro-scale electrostatic attraction and rapid phase separation. **b** Experimental EPR profiles (black) and quantum-chemical spectral fittings (red) of BioMFM monitored across three distinct chemical boundaries: solid-state powder, aqueous dispersion, and polar PNIPAM hydrogel precursor matrix. The rigid stability of the Landé splitting factor ([*g*] = 2.0032-2.0034) indicates retention of the defect-associated EPR signature across these chemical environments.



Supplementary Figure 50 Stimuli-responsive rheological transitions and network reversibility of the hydrogel matrices. a Temperature-dependent frequency-sweep profiles tracking the storage modulus (G′, filled symbols) and loss modulus (G″, open symbols) across the PNIPAM LCST, demonstrating thermally modulated viscoelasticity associated with the volume-phase transition. **b** Viscoelastic loss factor (tan δ) responses as a function of angular frequency, highlighting the temperature-modulated relaxation networks. **c** Overlapping frequency sweeps at 25 °C verifying the pristine mechanical and structural reversibility of the thermosensitive matrix following thermal cycling. **d** Frequency-dependent G′ and G″ profiles recorded under discrete glucose concentrations (0, 10, and 50 mM), showing the characteristic modulus crossover behavior of the dynamic covalent network. **e** Shifting tan δ trajectories tracking the glucose-responsive modulation of the polymer relaxation spectrum. **f** Reversibility evaluation via overlapping frequency-sweep spectra comparing the initial and chemically recovered states at 0 mM glucose.



Supplementary Figure 51 Multimodal glucose-responsive magnetic reconfiguration and rheological characterization of BioMFM hydrogels. a–d MFM phase mapping of phenylboronic acid–diol (PBA–diol) hydrogels highlighting glucose-induced domain reconfiguration (scale bar, 3 μm). **a** Neat PBA–diol network without BioMFM showing negligible phase contrast, confirming the absence of an intrinsic magnetic signal in the polymer matrix. **b** A 1 wt% BioMFM–PBA–diol hydrogel before glucose exposure displaying dispersed magnetic domains (phase range 0.2°). After equilibration in **c** 5 mM and **d** 10 mM glucose, the hydrogel exhibits increasingly pronounced, elongated red/blue features with the phase range expanding to ±0.7°. This transition is consistent with glucose-induced redistribution and clustering of BioMFM domains within the responsive network, providing a mechanism for untethered biochemical sensing. **e** Optical images of injectable BioMFM-sodium-alginate (NaAlg) hydrogels (0-10 wt% BioMFM) extruded through a clinical syringe, demonstrating consistent filament formation and facile percutaneous delivery. **f** Viscosity–shear-rate curves for BioMFM-NaAlg hydrogels revealing shear-thinning behavior across all concentrations, essential for maintaining structural integrity during minimally invasive deployment onto organ surfaces.

Supplementary Table 1 Comparative benchmarking of the BioMFM system against predominant bioelectronic monitoring modalities.

Modality	Advantage	Limitation	Ref.
BioMFM System	● Deep-Tissue Transduction Transparency ● Motion-Resilient Spatiotemporal Reconstruction ● Inherent Bioresorbability ● Mechanical Compliance	● Distance Sensitivity ● Resorption-Governed Operational Window	**This work**
Wearable Ultrasound Patches	● High-Resolution Deep-Tissue Imaging ● Non-Invasive Deployment ● Real-Time Hemodynamic Profiling	● Acoustic Coupling Fragility ● Motion-Induced Artifacts ● Energy-Intensive Sensing ● Compromised Comfort for Prolonged Wear	5–8
LC Resonant Sensors	● Passive, Battery-Free Operation ● Inherent Bioresorbability ● Architectural Simplicity for Minimally Invasive Implantation	● Distance/Alignment Sensitivity ● Single-Site Scalar Sensing Limitation (Pressure/Temp) ● Intrinsic Cross-Sensitivity and Crosstalk	9–11
Implantable Pressure Sensors	● High-Fidelity Hemodynamic Gold Standard ● Proven Clinical Utility for Direct Intracardiac Monitoring	● Single-Site Scalar Sensing Limitation (Pressure) ● Baseline Drift in Biofluid Environments ● Mechanical Mismatch Inducing Tissue Stress and Fibrosis	8,12–16
Optical PPG Devices	● High-Temporal-Resolution for Pulsatile Waveform ● Seamless Mechanical Integration via Flexible Electronics	● Penetration Limits due to Tissue Scattering and Absorption ● Baseline Drift from Refractive Index Mismatch ● Vulnerable Opto-Mechanical Coupling	11,17–19

Supplementary Table 2 Elemental composition of BioMFM determined by inductively coupled plasma–optical emission spectroscopy (ICP-OES).

Sample Mass	Final Volume	Target Element	Dilution Factor	Elemental Concentration of the Digestion Solution	Sample Elemental Content	Sample Elemental Content	Average content
M_0 (g)	V_0 (mL)		f	C_1 (μg/L)	C_x (μg/kg)	(ppm)	(ppm)
0.1299	25	Cr	1	17.131	3264.316	3.264316	3.2687392
				17.029	3244.888	3.244888	
				17.303	3297.014	3.297014	
		Mn		11.866	2261.139	2.261139	2.4398222
				13.134	2502.727	2.502727	
				13.412	2555.600	2.5556	
		Fe		98.173	18706.764	18.70676	18.794298
				97.881	18651.109	18.65111	
				99.843	19025.021	19.02502	
		Co		2.629	500.924	0.500924	0.5355107
				2.820	537.321	0.537321	
				2.982	568.287	0.568287	
		Ni		7.293	1389.747	1.389747	1.3984991
				7.334	1397.500	1.3975	
				7.391	1408.251	1.408251	
Total elemental*							26.4369

* $M_{s,\ impurity} \approx 0.0058$ emu g^{-1}; this theoretical ceiling is approximately 1,590 times lower than the experimentally verified saturation magnetization of BioMFM (M_s = 9.25 emu g^{-1} at 300 K).

Supplementary Table 3 Comparison of Curie temperature and saturation magnetization for representative metal-free molecular ferromagnets and metallic inorganic ferromagnets.

Materials	T_c (K)	M_s (emu g^{-1})	Year	Ref.
Pyrolytic Graphite	764	0.0022	2009	[20]
Stretched Teflon	300	0.0003	2012	[21]
Hydro-Graphene	300	0.006	2013	[22]
Defected C_3N_4	350	0.0076	2014	[23]
N-doped Graphene	678	0.148	2016	[24]
Poly (triazine imide)	300	0.015	2017	[25]
P-BNNSs	350	0.143	2017	[26]
Polymerized TCNQ	495	0.0032	2018	[27]
h-CBN	300	0.033	2019	[28]
1,3,5-Triazine	465	0.027	2019	[29]
F-Graphdiyne	300	0.17	2023	[30]
B-C_3N_4	550	0.035	2023	[31]
Crystalline C_3N_4	300	0.01	2024	[32]
Sp^2C-COF	300	0.0086	2025	[33]
Ni	627	55.1	1971	[34]
MnBi	628	79	2019	[35]
$Ni_{80}Fe_{20}$	820	89	2020	[36]
NdFeB	580	165	2022	[37]
MnSb	587	110	2023	[38]
Fe-Co-Ni	533	145	2025	[39]
BioMFM	480.1	9.25	2026	**This work**

Supplementary Table 4 *Stoner* analysis of itinerant ferromagnetism in BioMFM-C–C•$_x$ motifs.

C-C•$_7$	C-C•$_6$	C-C•$_5$	C-C•$_4$	C-C•$_3$	C-C•$_2$	C-C•$_1$	**BioMFM-C–C•$_x$**
0	0.5305	0.9524	0.1162	1.0	1.7093	1.0	**Magnetic Moment (μ_B)**
-	-0.243	-0.24	-0.095	-0.3812	-0.35	-0.4188	**$\triangle E$**
-	0.01	0.01764	0.00211	0.01786	0.02999	0.01724	**$\triangle m$**
-	0.3438	0.2387	0.1604	0.3698	0.6889	0.3860	**DOS (E_F/atom)**
-	24.32	13.6054	45.099	21.34	11.67	24.2956	**I_S (eV/μ_B)**
-	8.36	3.25	7.23	7.89	8.04	9.378	**|DOS (E_F)·I_S|**
0	4.108	7.234	0.866	7.317	12.282	7.058	**M_s (emu g^{-1})**

Supplementary Video 1 Macroscopic demonstration of spontaneous room-temperature ferromagnetism in BioMFM. This movie shows the metal-free molecular magnet BioMFM under ambient conditions, illustrating that its spontaneous magnetization at room temperature is strong enough to generate visible, macroscopic magnetic responses. The BioMFM powder was observed to undergo magnetically driven rigid-body motion and stable alignment with the nearby magnet in the absence of any mechanical attachment.

Supplementary Video 2 Bloomable BioMFM implant transitioning from closed delivery state to deployed configuration. This movie shows a foldable BioMFM patch undergoing reversible shape transformation from a compact, closed state to an open, bloom-like configuration, illustrating its suitability for minimally invasive delivery and conformal deployment on tissue surfaces. The pre-folded, rose-petal BioMFM construct was initially held in a sheath-like constraint mimicking a catheter or needle lumen. Upon sheath retraction, the patch was observed to rapidly bloom within seconds, with individual petals unfolding radially to enlarge the projected contact area.

Supplementary Video 3 Continuous spatiotemporal myocardial dynamic mapping with a BioMFM system. This movie shows the BioMFM system during in vivo operation in a porcine model, illustrating real-time tracking of myocardial contraction via transcutaneous magnetic sensing. The internal BioMFM implant was driven by local myocardial deformation and was inferred to generate time-varying magnetic flux that traversed the closed thoracic wall and was captured by the external Hall sensors, enabling continuous readouts of intrinsic myocardial dynamics without acoustic coupling, vascular access, or optical alignment. The time-domain streams were transmitted wirelessly to a smartphone-linked reader and a cloud-based analytics platform.

Supplementary Video 4 MRI verification (Day 28) of stable epicardial BioMFM implant deployed on a porcine myocardium. This video shows cardiac MRI in a porcine model, illustrating the epicardial position and long-term stability of the internal BioMFM patch. A single short-axis view through the left ventricle was acquired as a multi-phase cine sequence and is played back in real time. Throughout repeated cycles of systolic contraction and diastolic relaxation, the BioMFM implant remained conformally deployed onto the epicardium without detachment or migration.

Supplementary Video 5 Ultrasound-guided percutaneous injection of BioMFM hydrogel. This video demonstrates the percutaneous delivery of the BioMFM hydrogel onto a porcine liver surface under B-mode ultrasound guidance. The footage is presented at 0.3× speed to resolve the dynamic injection process. The entering syringe needle is visible as a bright, hyperechoic trajectory advancing towards the target interface. The emerging BioMFM hydrogel bolus appears as a distinct, localized hyperechoic region (due to acoustic impedance mismatch) contrasting against the underlying, relatively hypoechoic liver parenchyma. This visual contrast ensures precise, minimally invasive placement of deep-tissue magnetic markers for the continuous, untethered monitoring of organ-scale dynamics, bypassing complex transcatheter navigation procedures.

Supplementary Video 6 Injectability and filament extrusion of BioMFM–sodium-alginate hydrogel. This video shows the continuous extrusion of BioMFM-integrated sodium-alginate (NaAlg) hydrogels across a range of loadings (0, 1, 5, and 10 wt%) using clinical syringes. All formulations exhibit stable filament formation and smooth flow through narrow-gauge nozzles without evidence of clogging or jet breakup. The preserved flow profile across increasing loading concentrations confirms that the

incorporation of BioMFM (up to 10 wt%) maintains the shear-thinning behavior essential for percutaneous delivery and minimally invasive diagnostic applications.

Supplementary References:

1. Krieger, J. B., Li, Y. & Iafrate, G. J. Construction and application of an accurate local spin-polarized Kohn-Sham potential with integer discontinuity: Exchange-only theory. *Phys. Rev. A* **45**, 101-126 (1992).
2. Al Ma'Mari, F. *et al.* Beating the Stoner criterion using molecular interfaces. *Nature* **524**, 69–73 (2015).
3. Ahmad, W., Simon, E., Chithrananda, S., Grand, G. & Ramsundar, B. ChemBERTa-2: Towards chemical foundation models. Preprint at https://arxiv.org/abs/2209.01712 (2022).
4. Henkelman, G., Arnaldsson, A. & Jónsson, H. A fast and robust algorithm for Bader decomposition of charge density. *Comput. Mater. Sci.* **36**, 354–360 (2006).
5. Lin, M. *et al.* A fully integrated wearable ultrasound system to monitor deep tissues in moving subjects. *Nat. Biotechnol.* **42**, 448–457 (2024).
6. Zhou, S. *et al.* Clinical validation of a wearable ultrasound sensor of blood pressure. *Nat. Biomed. Eng.* **9**, 865–881 (2025).
7. Zhou, S. *et al.* Transcranial volumetric imaging using a conformal ultrasound patch. *Nature* **629**, 810–818 (2024).
8. Wu, J. *et al.* Adhesive anti-fibrotic interfaces on diverse organs. *Nature* **630**, 360–367 (2024).
9. Lan, Y. *et al.* Soft biodegradable implants for long-distance and wide-angle sensing. *Nature* **649**, 366–374 (2026).
10. Li, J. *et al.* An ultrasensitive multimodal intracranial pressure biotelemetric system enabled by exceptional point and iontronics. *Nat. Commun.* **15**, 9557 (2024).
11. Li, P., Hibino, N., Shi, L. L. & Tian, B. Minimally invasive bioelectronic implants. *Nat. Mater.* https://doi.org/10.1038/s41563-026-02576-9 (2026).
12. Kim, G. H., Uriel, N. & Burkhoff, D. Reverse remodelling and myocardial recovery in heart failure. *Nat. Rev. Cardiol.* **15**, 83–96 (2018).
13. Senga, R. *et al.* Atomic structure and dynamic behaviour of truly one-dimensional ionic chains inside carbon nanotubes. *Nat. Mater.* **13**, 1050–1054 (2014).
14. Oxley, T. J. *et al.* Minimally invasive endovascular stent-electrode array for high-fidelity, chronic recordings of cortical neural activity. *Nat. Biotechnol.* **34**, 320–327 (2016).
15. Inoue, T., Terada, N., Kobayashi, T. & Ogawa, O. Patient-derived xenografts as in vivo models for research in urological malignancies. *Nat. Rev. Urol.* **14**, 267–283 (2017).
16. Handorf, A. M., Zhou, Y., Halanski, M. A. & Li, W.-J. Tissue stiffness dictates development, homeostasis, and disease progression. *Organogenesis* **11**, 1–15 (2015).
17. Han, S. I. *et al.* Next-generation cardiac interfacing technologies using nanomaterial-based soft bioelectronics. *ACS Nano* **18**, 12025–12048 (2024).
18. Dcosta, J. V., Ochoa, D. & Sanaur, S. Recent progress in flexible and wearable all organic photoplethysmography sensors for SpO2 monitoring. *Adv. Sci.* **10**, 2302752 (2023).
19. Wu, W., Li, L., Li, Z., Sun, J. & Wang, L. Extensible integrated system for real-time monitoring of cardiovascular physiological signals and limb health. *Adv. Mater.* **35**, 2304596 (2023).
20. Červenka, J., Katsnelson, M. I. & Flipse, C. F. J. Room-temperature ferromagnetism in graphite driven by two-dimensional networks of point defects. *Nat. Phys.* **5**, 840–844 (2009).
21. Ma, Y. W. *et al.* Room temperature ferromagnetism in Teflon due to carbon dangling bonds. *Nat. Commun.* **3**, 727 (2012).
22. Eng, A. Y. S. *et al.* Searching for magnetism in hydrogenated graphene: using highly hydrogenated graphene prepared via birch reduction of graphite oxides. *ACS Nano* **7**, 5930–5939 (2013).
23. Gao, D. *et al.* Defect-related ferromagnetism in ultrathin metal-free g-C_3N_4 nanosheets. *Nanoscale* **6**, 2577–2581 (2014).
24. Miao, Q. *et al.* Magnetic properties of N-doped graphene with high Curie temperature. *Sci. Rep.* **6**, 21832 (2016).

25. Liu, L. *et al.* Enhanced room-temperature ferromagnetic properties in ultrathin two-dimensional metal-free poly (triazine imide) nanosheets. *Carbon* **124**, 486–491 (2017).
26. Lv, J., Sun, C., Ma, F., Wu, Y. & Shao, Y. Ferromagnetism of p-doped BN nanosheets prepared by red phosphorus assisted ball-milling exfoliated technique. *J. Mater. Sci. Mater. Electron.* **28**, 13149–13156 (2017).
27. Mahmood, J. *et al.* Organic ferromagnetism: trapping spins in the glassy state of an organic network structure. *Chem* **4**, 2357–2369 (2018).
28. Fan, M. *et al.* Doping nanoscale graphene domains improves magnetism in hexagonal boron nitride. *Adv. Mater.* **31**, 1805778 (2019).
29. Phan, H. *et al.* Room-temperature magnets based on 1, 3, 5-triazine-linked porous organic radical frameworks. *Chem* **5**, 1223–1234 (2019).
30. Lin, L., Ye, X., Pan, H., Li, F. & Du, Y. Induced room-temperature ferromagnetism in graphdiyne by a synergistic effect of out-of-plane F and OH dual-doping. *Chem. Mater.* **35**, 9552–9561 (2023).
31. Du, L., Gao, B., Xu, S. & Xu, Q. Strong ferromagnetism of g-C_3N_4 achieved by atomic manipulation. *Nat. Commun.* **14**, 2278 (2023).
32. Wang, Y. *et al.* Room-temperature ferromagnetism and piezoelectricity in metal-free 2D semiconductor crystalline carbon nitride. *Nano Res.* **17**, 5670–5679 (2024).
33. Li, S. *et al.* Synthesis of single-crystalline sp^2-carbon-linked covalent organic frameworks through imine-to-olefin transformation. *Nat. Chem.* **17**, 226–232 (2025).
34. Crangle, J. & Goodman, G. M. The magnetization of pure iron and nickel. *Proc. R. Soc. Lond. A Math. Phys. Sci.* **321**, 477–491 (1971).
35. Jensen, B. A. *et al.* Optimizing composition in MnBi permanent magnet alloys. *Acta Mater.* **181**, 595–602 (2019).
36. Holanda, J. *et al.* Magnetic damping modulation in $IrMn_3/Ni_{80}Fe_{20}$ via the magnetic spin Hall effect. *Phys. Rev. Lett.* **124**, 087204 (2020).
37. He, Y. *et al.* Nanoscale magnetic bubbles in $Nd_2Fe_{14}B$ at room temperature. *Phys. Rev. B* **105**, 064426 (2022).
38. Dara, H. K., Harikrishnan, R., Bitla, Y. & Babu, P. D. Disorder induced cluster spin glass like state in MnFeSb. *J. Magn. Magn. Mater.* **583**, 170990 (2023).
39. Li, B. *et al.* Stress relief annealing of super Invar alloy: Microstructure, soft magnetic and thermal expansion properties. *J. Alloys Compd.* **1010**, 177975 (2025).